

Magneto-thermoelectric effects in magnetic metallic thin-films

**Von der Fakultät Maschinenwesen
der Technischen Universität Dresden
zur Erlangung des akademischen Grades
Doktoringenieur (Dr.-Ing.)
angenommene**

Dissertation

M.Eng. Park, Gyuhyeon

geb. am: 18.10.1986 in Seoul, Südkorea

Tag der Einreichung:	01. März 2021
Tag der Verteidigung:	20. Mai 2021
Gutachter:	Prof. Dr. rer. nat. Kornelius Nielsch Prof. Dr. Gianarelio Cuniberti Prof. Wooyoung Lee Ph.D
Vorsitzender der Promotionskommission:	Prof. Dr. -Ing. Christoph Leyens

© 2021

All Rights reserved

GYUHYEON PARK

Magneto-thermoelectric effects in magnetic metallic thin-films



Abstract

The purpose of this thesis was to evaluate two-dimensional (2D) magneto-thermoelectric (MTE) phenomena in a thinner regime. Primarily, this work was motivated by the recent discovery of MTE properties in transition metal dichalcogenides (TMDs). In general, TMD thin films have attracted much attention due to their very good electrical, optical, and electrochemical properties. However, the total number of studies of the MTE phenomena in TMDs is rather small compared to other properties, such as electric, optoelectric, and catalyst properties. Hence, in this thesis, we aimed to evaluate the MTE properties in TMD materials. Before we started to measure TMDs, we established a measurement platform and studied MTE properties in ferromagnetic CoFeB, and Weyl semimetal Co₂MnGa.

The first part of this thesis will explain the general physical background, the fabrication methods and the data evaluation. For example, in Chapter 1, the physical background of the Seebeck effect, the anomalous Hall effect, and the anomalous Nernst effect will be introduced. Chapter 2 contains the sample preparation methods by physical vapor deposition, mechanical exfoliation and the lithography process. Chapter 3 describes general data evaluation methods.

Chapter 4 highlights a comprehensive summary of the state-of-the-art research on TMD films and observes recent applications of these materials in electronic transport, optoelectronics, energy, memory, thermoelectric and MTE.

Furthermore, it summarizes the important properties within each application. Additionally, an extended version was written by the author and published as: *G. Park, K. Nielsch, A. Thomas: 2D transition metal dichalcogenide thin films obtained by chemical gas phase deposition techniques, Adv. Mater. Inter. 6 (2019) 1800688*

In Chapter 5, we establish the measurement platform to measure the MTE properties. Furthermore, this chapter shows the anomalous Hall effect and the anomalous Nernst effect properties with sputtered CoFeB thin films of 60 nm thickness and reveals ferromagnetic behavior in this thinned regime. A publication with the main experimental contributions by the author is published as:

H. Reichlova, R. Schlitz, S. Beckert, P. Svekis, A. Markou, Y.-C. Chen, D. Kriegner, S. Fabretti, G.H. Park, A. Niemann, S. Sudheendra, A. Thomas, K. Nielsch, C. Felser, S.T.B. Goennenwein: Large anomalous Nernst effect in thin films of the Weyl semimetal Co_2MnGa , Appl. Phys. Lett. 113 (2018) 212405.

In Chapter 6, we evaluate the AHE and the ANE with cosputtered Co_2MnGa thin films with various thicknesses from 20 nm to 50 nm using our own platform. In addition, we evaluate the anomalous thickness behavior, which reveals that at lower thickness regimes, intrinsic effects are more feasible than Berry curvature. In addition, another publication was written by the author and published as:

G.-H. Park, H. Reichlova, R. Schlitz, M. Lammel, A. Markou, P. Svekis, P. Ritzinger, D. Kriegner, J. Noky, J. Gayles, Y. Sun, C. Felser, K. Nielsch, S.T.B. Goennenwein, A. Thomas: Thickness dependence of the anomalous Nernst effect and the Mott relation of the Weyl-semimetal Co_2MnGa thin films, PRB 101, 060406(R) (2020).

In Chapter 7, we evaluate the AHE and the magnetic character in a TMD VS_2 flake. The flake shows a temperature dependence and reveals two Curie temperatures that represent charge density wave like behavior at approximately 100 K and a magnetic phase transformation at approximately 20 K. Furthermore, we found an external magnetic field dependence in the magnetoresistance and an anomalous Hall signal at a lower temperature regime from 20 K. Specifically, the measured magnetoresistance and anomalous Hall effect have a small hump at 2.5 T and exhibit below 20 K as a base temperature.

1. Introduction

- a. Physical background
 - i. Seebeck effect
 - ii. Anomalous Hall effect and anomalous Nernst effect
 - iii. Mott relation

2. Sample preparation and evaluation

- a. Physical vapor deposition
- b. Mechanical exfoliation
- c. Patterning process

3. Data evaluation

4. State of the art in transition metal dichalcogenids

- a. Introduction
- b. TMDs in use
- c. Magneto-thermoelectric properties of TMDs

5. Magneto-thermoelectrical properties in CoFeB thin film

- a. Introduction
- b. Results and discussion
- c. Conclusions

6. Anomalous Nernst and anomalous Hall effects in Co_2MnGa thin films

- a. Introduction
- b. Results and discussion
- c. Summary

7. Anomalous Hall effect in exfoliated VS_2 flakes

- a. Introduction
- b. Experiments
- c. Results and discussion
- d. Summary

8. Summary

Acknowledgments and References

1. Introduction

a. Physical background

i. Seebeck effect

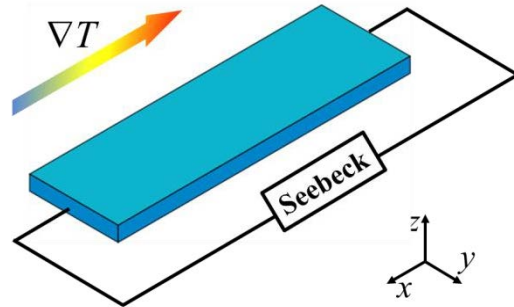


Fig. 1 A schematic diagram of the Seebeck effect.

In 1821, Thomas Seebeck observed that when two dissimilar materials (copper and bismuth wires) are joined together and the junctions are held at different temperatures (T and $T+\nabla T$), a voltage difference (ΔT) develops that is proportional to the temperature difference (ΔT). For an intrinsic property of the material, Seebeck can be expressed by the following equation [1]:

$$\vec{j} = \sigma(\nabla V - S\nabla T)$$

where \vec{j} is the electrical current density, and σ is the electrical conductivity. Once the temperature gradient ∇T along the x -direction is applied, the charge carriers in the sample diffuse down the gradient and accumulate at the boundaries.

This generates an electric field $E_x = \nabla V$ that generates a drift of charge carriers that balances the current driven by ∇T_x . Therefore, the total current density \vec{j} is zero and $\sigma \nabla V_x - \sigma S \nabla T_x = 0$; as a result, $S_x = \nabla V_x / \nabla T_x$. A schematic of the Seebeck effect is shown in Fig. 1.

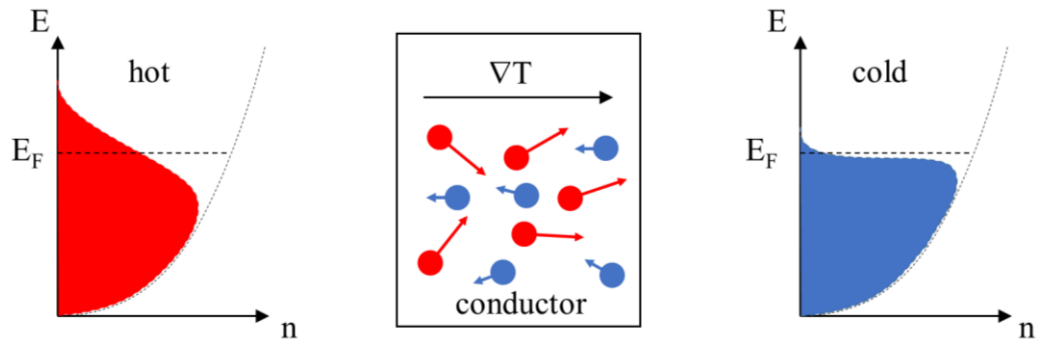


Fig. 2 Schematic diagram of the Seebeck effect when a temperature gradient is applied to a conductor. The density of the states is plotted as a function of the energy for the hot and cold ends of the conductive medium.

The Seebeck effect stems from the idea that the conductivity for the electron is energy dependent. The electron distribution over the energy states and the density of states $g(E)$ scales with \sqrt{E} , as described by the Fermi-Dirac statistics. At the hot end, the electrons are pumped out over higher energy states due to the temperature dependence as shown in Fig. 2. Consequently, the average energy per electron is larger than that for electrons in the cold region. As a result, the net flow of energy remains because electrons that diffuse from the hot end to the cold end therefore have more energy than the electrons that diffuse in the opposite direction, leading to a net flow of energy. This process can be explained essentially by the thermal

conductivity of electrons. When the electrical conductivity of the high- and low-energy electrons is the same, both charge currents are trivial; consequently, there is no net charge movement. However, a net diffusion of charge occurs when electrons with higher energies experience a different conductivity than electrons with lower energies. In an equilibrium state, this process is restricted by an electric field that builds up and intercepts further diffusion. In the end, we named this electric field the Seebeck effect [2].

ii. Anomalous Hall effect and anomalous Nernst effect

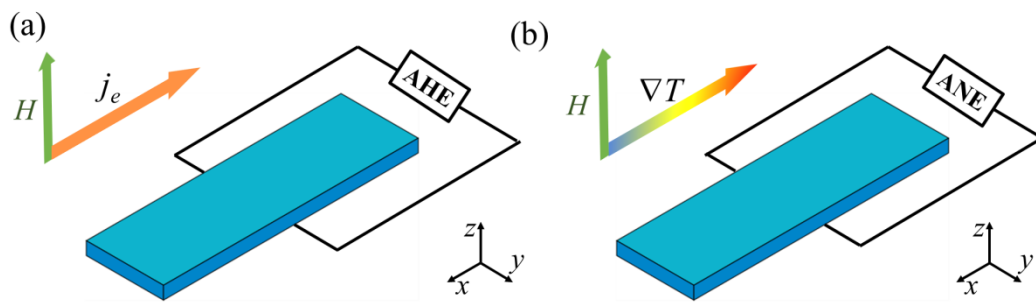


Fig. 3 Schematic diagram of (a) the anomalous Hall effect and (b) the anomalous Nernst effect.

In 1879, Edwin H. Hall proposed the ordinary Hall effect (OHE), i.e., that a small transverse electric field (E_H) is proportional to the product of the primary current density (I_D) and a component of the magnetic field flux (B_Z) [3]. Therefore, the OHE can be expressed as:

$$E_H = RI_D B_Z$$

where R is the Hall coefficient. However, there is a response to spontaneous magnetization, which is no longer proportional to the applied field in ferromagnetism. We call it the anomalous Hall effect (AHE). Accordingly, the Hall resistivity (ρ_{xy}) has an empirical relationship that is expressed as a sum of the resistivity corresponding to AHE (ρ_{xy}^{AHE}) and the resistivity corresponding to the ordinary Hall effect (ρ_{xy}^{OHE}) as shown below.

$$\rho_{xy} = \rho_{xy}^{OHE} + \rho_{xy}^{AHE} = R_0 B_Z + R_S M$$

where B_Z is the applied magnetic field, M is magnetization, and R_0 and R_S are the ordinary and anomalous Hall coefficients, respectively. This empirical relation between the magnetization and Hall resistivity was independently reported by Smith and Pugh, four decades after the discovery of AHE [4-6].

The origin of the AHE can be explained by two compositions: intrinsic and extrinsic Hall effects. The intrinsic AHE was studied by Karplus and Luttinger from intrinsic spin-orbit interactions for itinerant spin polarized electrons. The study suggested the acquisition of group velocity for electrons with an external electric field [7]. This anomalous velocity contributes to the Hall effects because of its perpendicularity to the electric field. In the case of a ferromagnetic conductor, the sum of the anomalous velocity can be nonzero and, thus, contribute to the transverse Hall conductivity. This contribution in the AHE depends on only the band and, thus, can be expressed completely in terms of the Bloch function of the host crystal. Anomalous Hall conductivity (AHC) is independent of the impurity

concentration [8-10], and it yields an AHE contribution of $\rho_{xy} \approx \sigma_{xy}/\sigma_{xx}^2$ and is therefore proportional to ρ^2 .

For a long time, it was believed that the AHC scales with the sample's magnetization. Accordingly, any ferromagnetic material shows an AHE, but it is zero for an antiferromagnet, owing to the compensation of the magnetic sublattices ($M = 0$). Hence, the AHE has been treated as an important signature of finite magnetization in ferromagnets or ferrimagnets. However, recently, it was realized that the intrinsic contribution to the AHE is not directly related to the sample magnetization of a material but derives more generally from its net Berry curvature [11].

The Berry curvature distribution in materials is a property of the band structure. The band structure determines the topological aspects of a material [7, 12-14]. The absence of time-reversal symmetries and a finite net Berry curvature are a necessary condition for a nonzero AHE. Notably, the time reversal symmetries reverse the sign of the local Berry curvature in the Brillouin Zone (BZ) when reversing the sign of the momentum vector. In the calculations, we can control the Berry curvature and intrinsic AHE by suitable manipulations of the symmetries and band structure which is independent of the finite value of the magnetization [15]. According to these considerations, a strong AHC was predicted in the noncollinear antiferromagnetic systems such as Mn_3Ir [16], Mn_3Ge , and Mn_3Sn [17], and then experimentally observed in Mn_3Ge [18] and Mn_3Sn [19, 20]. Furthermore, very recently, a large intrinsic AHE has been found in magnetic Weyl semimetals with a broken time-reversal symmetry that depends on the separation of the Weyl

nodes in momentum space [21-25]. As an example, the Weyl point acts as the monopole of the Berry curvature, where a topological invariant, the Chern number, can be assigned to each Weyl node in Weyl semimetals [26, 27]. Thus, we can tune the AHC via the symmetry and topological band structure without considering the net magnetic moments [28]. The schematic in Fig. 3 (a) describes the AHE.

The anomalous Nernst effect (ANE), is the thermal counterpart of the AHE. One of the key effects in spin-caloritronic research is experimentally observed as a transverse voltage generated in a magnetic material subjected to a thermal gradient. The ANE was considered to be proportional to the magnetization. However, recent studies suggest that Berry curvature effects can play a dominating role. The exact origins of both the AHE and ANE have been actively discussed [29]. In general, the extrinsic and intrinsic (Berry phase) contributions are mostly understood. It has been assumed that the ANE is dominated by the net Berry curvature of all bands near the Fermi level [30-32] in some materials. Furthermore, the AHE and the ANE can be apprehended via the Mott relation [33]. The schematic in Fig. 3 (b) describes the ANE.

iii. Mott relation

The Mott relation is an explanation that is applicable in materials where each charge carrier follows an essentially static environment in such a way that its motion can be described independently from other carriers and other dynamics [34].

In other words, the Mott relation can be applied in materials where each charge carrier acts independently [34].

The AHE and the ANE are connected via the Mott relation. In general, the Seebeck effect is well described based on the Mott relation via the following:

$$S = \frac{\pi^2 k_B^2 T}{3e\sigma} \left(\frac{\partial \sigma}{\partial E} \right)_{E_F}$$

where k_B is the Boltzmann constant, e is the elementary charge, and E is the energy derivative of the σ electrical conductivity at the Fermi level (E_F). The sign and magnitude of the induced electric field is represented by the Seebeck coefficient. Additionally, the Mott relation holds to explain the dominant intrinsic character in the anomalous transport in ferromagnetic materials [35]. Furthermore, the Seebeck coefficient (S_{xx}) is related to other transport coefficients by

$$S_{yx} = \frac{1}{\sigma_{xx}} (\alpha_{yx} - \sigma_{yx} S_{xx})$$

where σ_{yx} is the transverse anomalous Nernst conductivity, σ_{xx} is the longitudinal resistivity, and S_{yx} is anomalous Nernst coefficient. This aspect will be discussed in Chapter 5 in more detail.

2. Sample preparation

a. Physical vapor deposition

Physical vapor deposition (PVD) techniques are a way to synthesize thin films. PVD gives intense energy input into a pure solid material to physically form a vapor that can condense on a surface in ultrahigh vacuum (UHV) or in a background ultrahigh purity gas [35]. UHV pressures are on the order of 1×10^{-8} mbar and are generally used in semiconductor material fabrication.

Magnetron sputtering uses a background gas introduced into an ultraclean UHV environment. Compared to other deposition processes, this process is rather simple. Argon gas is generally used as the background gas at low pressures with a target material of ultrahigh purity attached to a magnetron sputter gun. When a sufficiently high potential is applied to the target surface, plasma is ignited by the background gas according to Paschen's law. The positively charged argon ions are accelerated into the negatively charged target and the solid material comprising the target is ejected toward the substrate [35]. This method deposits the material on the surface of the substrate within the vacuum chamber, and the target material is grown with this technique [36].

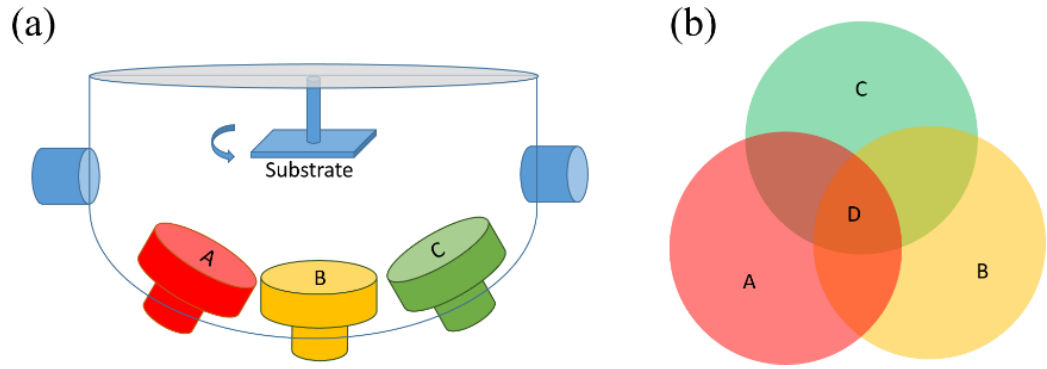


Fig. 4 Schematics for (a) a co-sputtering chamber and (b) variation in the deposition area.

In this study, sputtering experiments were performed in a multisource Bestec UHV magnetron sputtering deposition system. Prior to deposition, the chamber was kept at a base pressure (8×10^{-9} mbar), while the process gas (Ar 5 N) continuously flowed into the chamber. The pressure was 3×10^{-3} mbar. For CoFeB thin films, a single the $\text{Co}_{40}\text{Fe}_{40}\text{B}_{20}$ target was used. On the other hand, for Co_2MnGa thin film, three different sources were used in confocal geometry as shown Fig. 4 (a). The substrate can be placed in the “D” regime where it is possible to deposit a composition of sources A, B, and C. In more detail, we will discuss this in Chapters 5 and 6.

b. Mechanical exfoliation

Mechanical exfoliation is a typical top/down method for making 2D materials, in which the driving forces can break the weak van der Waals interaction

between the layers in bulk layered materials. Since the first demonstration in one-atom-thick graphene was exfoliated by scotch tape, this easy yet approachable exfoliation method has served as a promising processing method for proof-of-concept demonstrations [37]. The advantage of this method is that it can produce high-quality samples, but they are very small. Therefore, the method can be applied only in fundamental research and prototypical devices. The sequential procedure is shown in Fig. 5.

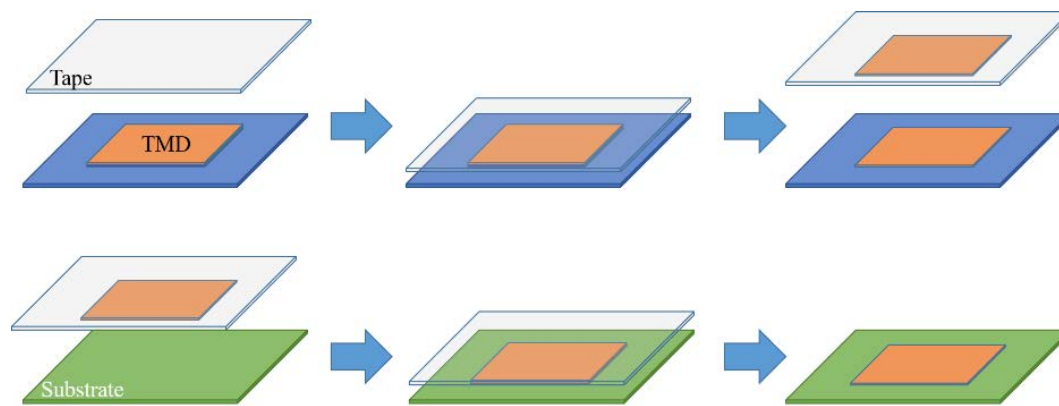


Fig. 5 Schematics for the mechanical exfoliation process.

c. Patterning process

The fabrication of magneto-thermoelectrical properties using thin films and flakes involves multiple physical and chemical processes performed on a substrate. Although silicon wafers are generally used in the semiconductor industry, glass- or MgO- like insulating materials without any junction effect have preferably were used in lab-scale fundamental research projects.

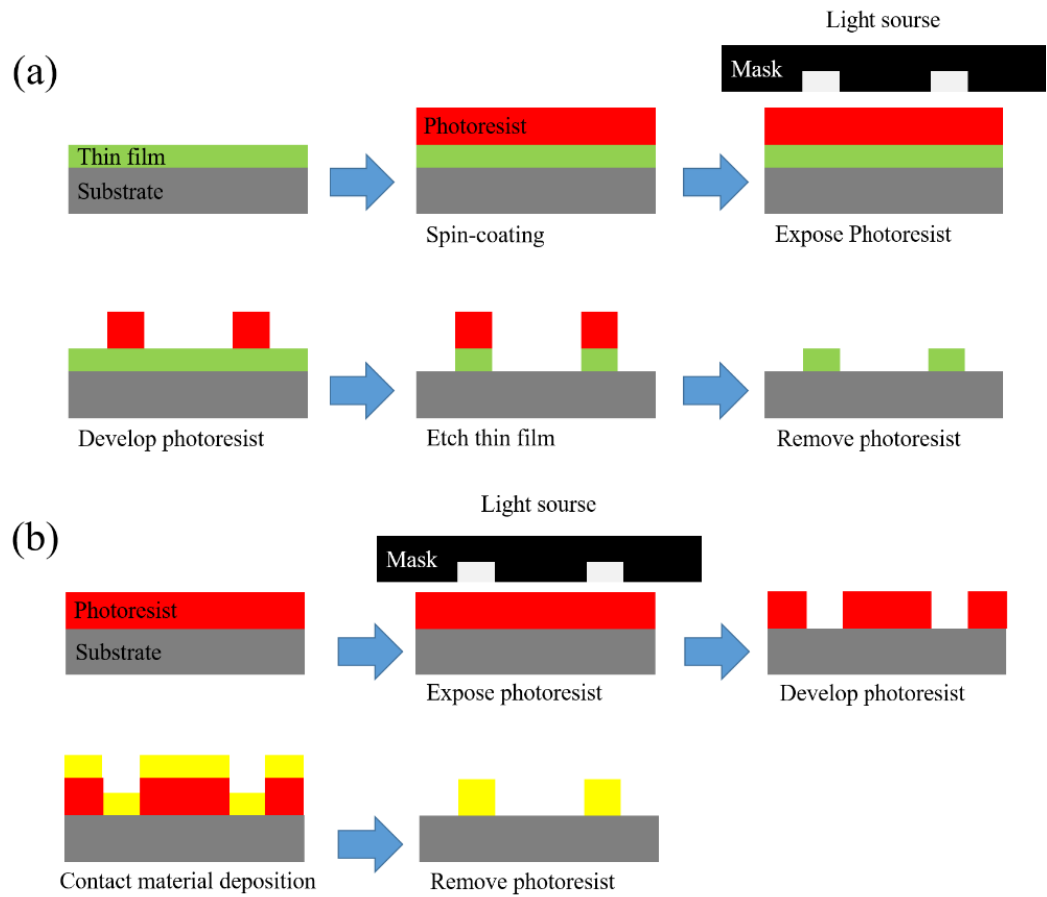


Fig. 6 Schematics for lithography. Patterning process for (a) Hall-bar structure and (b) metal contacts as thermometers, heaters, and contacts.

Here we explain the steps to prepare the devices. Firstly, clean the substrate was cleaned with acetone and ultrasonicated for 5 min. Then, the substrate was dehydrogenated by placing it on a hot plate at 453 K for 1hour. At this step, we can remove improper dust or organic contamination. Second, we coat the substrate homogenously with a spin coater with proper speed rotation, and then prebake if needed. Third, the prepared patterned was exposed to the photoresist, and the development process was performed. In this process, the disclosed place generates

both physical and chemical transformations to the photoresist. During the development process, the regions that were exposed to light can be developed/grown (negative photoresist) or removed (positive photoresist) after this process. The sequential procedure is presented in Fig. 6 (a).

Afterward, with the Hall-bar structured sample, the metal contact part can be prepared, for example, heaters, thermometers, and contacts, to gather the transporting signal. Therefore, a second procedure to fabricate the metal contacts is necessary and is described in Fig. 6 (b). Generally, Pt or Au is used for the metal contacts due to their high electrical and thermal response, and they can be prepared by sputtering.

3. Data evaluation

Generally, to evaluate the electrical transport properties, the patterned Hall bar structure and an additional on-chip heater strip are needed to generate the thermal gradient and monitor the thermoelectric and magnetotransport signals. At same time, Pt or Au metals, i.e., conducting materials are generally used for thermometer, heaters and contacts to record the electrical signals. Normally, the sample's base temperature where we are interested can be tuned by a cryostat device that is cooled down to a low temperature using a cryogenic fluid bath such as liquid helium. Additionally, we can apply an external magnetic field at a given temperature, thus enabling us to quantify the AHE, ANE, and Seebeck effect.

In Fig. 7, the schematic for the AHE is represented. In more detail, the longitudinal current I_x under a perpendicular external magnetic field H_z contributed to the transversal voltage V_y . Specifically, the electrons with majority and minority spin, which arise from spontaneous magnetization and have opposite “anomalous velocity” due to spin-orbit coupling, then cause an unbalanced electron concentration at the two transversal sides, which leads to a finite

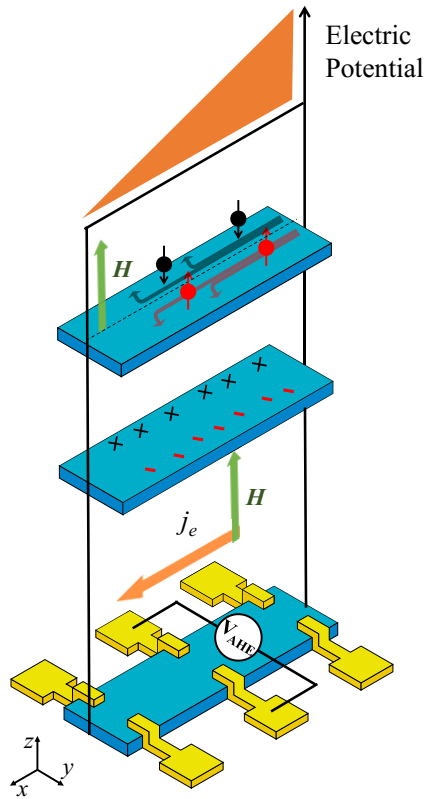


Fig. 7 A schematic of the AHE.

voltage V_y . Consequently, the contacts recording the AHE signal were placed along the y-(transverse) direction. To evaluate the AHE, in this study, we applied a current (I_{xx}) and measured the transverse (V_{xy}) and longitudinal (V_{yx}) voltages with an external magnetic field ($\mu_0 H$) in the perpendicular direction. Notably, the Hall resistivity ρ_{yx} is usually recorded [38] with a metal contact. Thus, we can evaluate the Hall conductivity (AHC) $\sigma_{xy} = \rho_{yx}/(\rho_{xx}^2 + \rho_{yx}^2)$ in theoretical calculations, where ρ_{xx} is the longitudinal resistivity, and ρ_{yx} is the transversal resistivity [21]. Notably, the longitudinal conductivity can be evaluated as $\sigma_{xx} = 1/\rho_{xx}$ [39]. Additionally, to independently record the AHE response of a sample, a DC current was applied along the Hall bar, and the transversal voltage was measured.

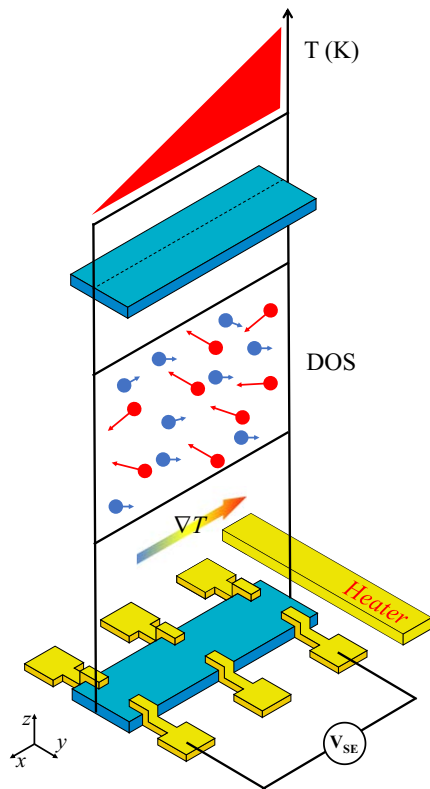


Fig. 8 A Schematic of the Seebeck effect.

In contrast to the AHE, the Seebeck effect is based on a thermoelectric signal, thus, a specific temperature gradient is obligatory [40]. In Fig. 8, the schematic for the Seebeck effect is represented. More specifically, because a thermal gradient is applied along the x-direction, the conductivity for the electron is generated due to the Seebeck effect. The density of the states is shown in the figure; the electrons are pumped out over higher energy states to the cold end due to thermal energy dependence. As mentioned before in Chap. 1,

in the physical background of the Seebeck effect, the electrons diffuse in the opposite direction from the hot to the cold ends, which leads to a net flow of energy. To generate the Seebeck effect, additional heaters were placed to generate a thermal gradient along the x-axis, as shown in Fig. 8. To evaluate the thermal gradient, we assume $\Delta T = \Delta T/L$, where ΔT is the temperature difference, and L is the distance between the points where the temperature is measured. Therefore, we can evaluate the Seebeck effect according to $S_x = \nabla V_x / \nabla T_x$.

The concept of the ANE is a combination of the AHE and the Seebeck effect as shown in Fig. 9. Notably, the ANE and the AHE share the origin of the contributions of the extrinsic and intrinsic mechanisms. For the ANE, the external magnetic field needs to be applied in a perpendicular direction in alignment with the z-axis. Notably, the thermal gradient can generate an electric current, and the additional applied current is not obvious. The anomalous Nernst coefficient N_{ANE} is evaluated as follows: $E_{ANE} = -S_{xy} m \times \nabla T$. In

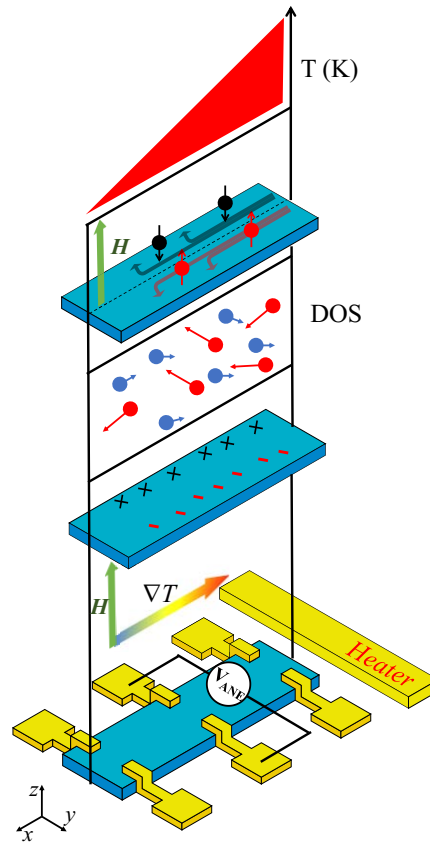


Fig. 9 A schematic of the ANE.

this expression, E_{ANE} and m are the electric field induced by the ANE and the magnetization vector, respectively.

4. State of the art in transition metal dichalcogenides

a. Introduction

Ultrathin 2D transition metal dichalcogenide (TMD) thin films have attracted much attention due to their very good electrical, optical, and electrochemical properties. Many properties of layered TMDs have been previously measured, such as electrical, magnetic, and optical properties, to aid in the development of high-performance materials and for many applications, such as in optoelectronic, electron transporting, and electrochemical devices [41].

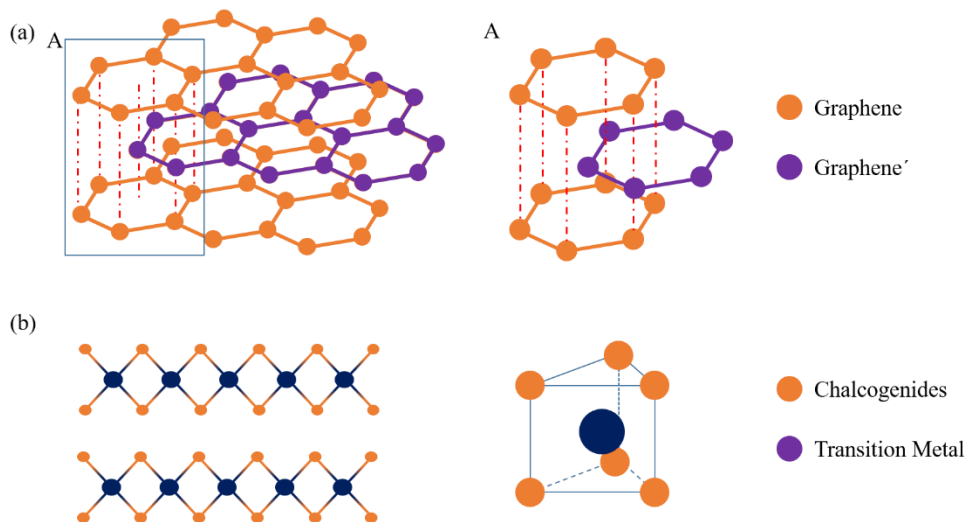


Fig. 10 Schematics for (a) graphene and (b) transition metal dichalcogenides.

Most 2D TMDs are composed of MX_2 units where M is a transition metal and X is a chalcogenide, e.g., sulfur, selenium, and tellurium. The structure of graphene, which has van der Waals (vdW) bonding between adjacent layers, is

shown in Fig.8 (a). Specifically, the sequential X–M–X layers in a multilayer sandwich exhibit weak vdW bonding between the adjacent layers, as shown in Fig. 10 (b). In this chapter, recent progress in 2D TMD thin films and the current magneto-thermoelectric properties are surveyed.

b. TMDs in use

TMDs show great potential in many advanced technological fields. The field pertaining to TMDs can be divided into four parts as a function of the TMD properties, namely, electronic transport, optoelectrics, energy, and future devices, as shown in Fig. 11. Furthermore, this are will be explained in more detail for each part in this chapter.

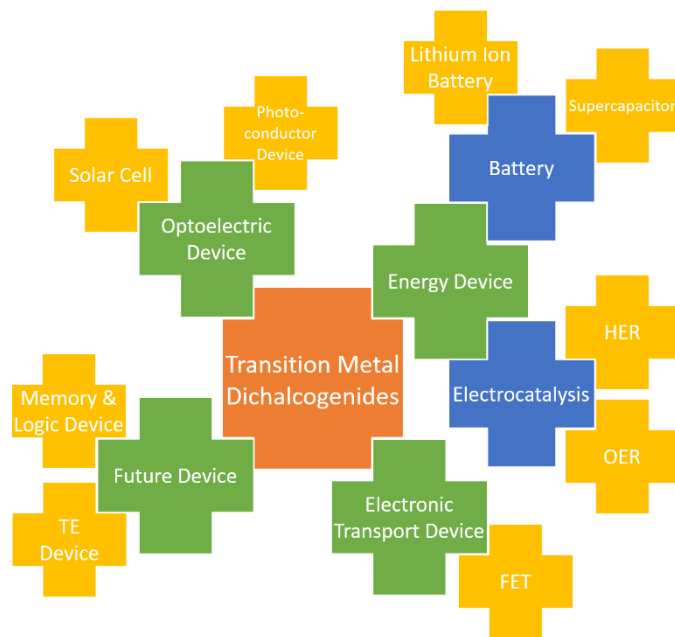


Fig. 11 Optoelectric, energy, electronic transport and future devices based on 2D transition metal dichalcogenides.

In particular, TMDs have interesting properties, such as flexibility, transparency, and tunable bandgaps, which silicon wafers cannot provide [42]. For example, their bandgaps range from 0 to ≈ 2.1 eV, and they are applied in high-performance field effect transistors (FETs) [43]. Considerable effort has been dedicated to achieving scalable synthesis of the high-quality 2D TMD thin films necessary for the development of FETs. Although the TMDs have potential for devices, it is still challenging to make practical connected devices with the desired charge carrier mobility. As a result, many studies focus not only on producing high-quality single-crystal mono- or few-layer materials but also on breaking the obstacles to minimizing their size. As seen in Table 1, the experimentally demonstrated charge carrier mobilities of mono- or few-layer TMDs are lower than the commercial needs and theoretical prediction [44].

Table 1 Summary of the properties of FETs with 2DMs.

Material	Type	On / Off ratio	Mobility [cm ² /Vs]	Layer thickness	Ref.
MoS ₂	n	10 ⁷	470	mono	45
MoSe ₂	n	10 ⁶	50	mono	46
MoTe ₂	p	10 ³	1	3.1 nm	47
NbS ₂	n	2.3×10 ³	12.7	2-8 layer	48
ReS ₂	n	10 ⁶	9.3	mono ~ bulk	49
VS ₂	n	10 ⁶	2-7.8	~10 nm	50
WS ₂	n	10 ⁶	5-18	mono	51
WSe ₂	p	10 ⁸	350	Mono, di	52
WTe ₂	n	10 ³	144	Mono~7 layer	53
ZrS ₂	n	10 ⁵	0.01-5	3-15 nm	54

Particular attention has been given to 2D layered semiconductors due to their unique photovoltaic and optoelectronic properties, which arise from their controllable bandgaps, which range from IR to visible and the UV range [55].

Optoelectronic devices are able to create, detect, and control light, including photovoltaic devices (solar cells) and photodetectors [56]. Furthermore, monolayered TMD materials often show a direct bandgap. This bandgap will increase their efficiency compared to indirect bandgap materials, because the absorption or emission of an additional phonon is not required [44].

TMDs offer light absorption and provide promise for large-area high-performance devices that are fabricated using scalable techniques. The property is necessary for solar cell devices. TMDs exhibit superior light harvesting characteristics in their bulk form due to their suitable bandgap energy and their high absorption coefficients ($10^5\sim 10^6\text{ cm}^{-1}$). Furthermore, when the thickness of TMDs decreases to a mono-layer or a double layer, because of quantum confinement effects, the bandgap is tunable, and the photovoltaic character can be drastically enhanced [57]. Moreover, atomic layer heterojunctions or vdW heterojunctions can be constructed without lattice strain, which can lead to defects and recombinations. It has also been shown that single- or few-layer TMDs exhibit superior light harvesting characteristics due to strong light–matter interactions from dipole-allowed localized d-state transitions [58]. In Table 2, we summarize the materials and the corresponding references and include the key parameters for solar cells.

Table 2 Summary of properties of solar cells with 2DMs.

Material	V _{OC} [V]	J _{SC} [mA cm ⁻²]	Fill factor (FF) [%]	PCE [%]	Ref.
CoS ₂	0.71	10.63	0.60	4.58	59
FeS ₂	0.70	10.67	0.60	4.46	59
MoS ₂	0.59	36.8	73	15.8	60
MoTe ₂	0.69	16	65.64	7.25	61
NiS ₂	0.73	10.34	0.62	4.75	59
TiS ₂	0.517	1.76	63.09	0.57	62
WS ₂	0.69	9.66	0.63	4.30	59

It is notable that 2D TMDs have attracted great interest in photoconductor devices. While there are many photoconductor materials available, the structure of a TMD layer has many similarities with graphene and it shows notable electrical characteristics such as a high on/off current ratio, carrier mobility, and photoresponse [44]. As mentioned before, TMDs have generally been applied for radiation detection in a wavelength range from ultraviolet (UV) to visible and near-infrared (vis–NIR), and their application can be divided into their detection ranges. Although 2D layered materials have good transparency, the materials can strongly interact with incident light, leading to enhanced photon absorption and electron–hole creation due to the existence of van Hove singularities in their electronic density of states [63].

Previous UV photodetectors based on Si, GaN, diamond, and AlGaIn show low responsivities of $\approx 0.1 \sim 0.2 \text{ mA W}^{-1}$, and a lattice mismatch remains between the semiconductor materials and the substrates, hindering device performance. Photodetectors for the vis (400–760 nm) and NIR (760–3000 nm) ranges are widely studied due to their application in communication media and biomedical science

[64]. However, Si-based commercial visible photodetectors exhibit disadvantages, such as crosstalk and high temperature processing [65]. For these reasons, as stated above, TMDs have been studied and have emerged as promising candidates to overcome these drawbacks.

Although several candidates, such as Mo-, Hf-, Zr-, Re, and W-based chalcogenides, have been investigated for photoelectronic devices, the improvement of properties, such as the responsivity, detectivity, and response time, is still needed to fulfill commercial requirements. In other words, the efficiency of TMD-based optoelectronics is still low. Some of the major issues arise from the thin nature of the materials, which prohibit sufficient light absorption, despite their high absorption coefficient ($\approx 10^7 \text{ m}^{-1}$ in the visible range) [66]. At the same time, employing a heterostructure is regarded as a potential solution, either by stacking multiple 2D TMDs or other 2DMs, such as graphene and boron nitride nanosheets, or stacking on other functional substrates [67]. The properties of photodetectors with 2DMs are summarized in Table 3.

Table 3 Summary of properties of photodetectors with 2DMs.

Material	Response spectrum [nm]	Responsivity [A W^{-1}]	Response time [ms]		Detectivity (D^*) or noise-equivalent power (NEP) [Jones]	Ref
			Rise	Decay		
HfS ₂	355-475	10^{-5}	0.13	0.155	7×10^8	68
MoS ₂	632	15.6	100	150		69
MoSe ₂	532-650	2.15×10^{-4}	<25	<25		70
ReS ₂	500-523	604	<2	<2	4.44×10^{10}	71
ReSe ₂	808	2.98	5×10^3	8×10^3		72
WS ₂	457-647	9.2×10^{-5}	5.3	5.3		73
WSe ₂	532	1.01	10^3			74
ZrS ₂	450-630	0.57				75

Currently, 2D TMDs are gaining significant attention as electrode materials for electrocatalysis and as energy devices, such as supercapacitors and Li-ion batteries for storage techniques, due to their atomically layered structure, high surface area, and excellent electrochemical properties [44]. For TMDs, active sites along the edges of their 2D layered crystal structure benefit their catalytic activities [56]. Moreover, chemically active TMDs store energy mainly through a fast and reversible redox reaction, while their large surface area and interlayer space facilitate ion intercalation [76].

In general, platinum-based materials and other noble metals or alloys are still the best electrocatalysts for the hydrogen evolution reaction (HER). However, the high cost of the raw material still limits its their large-scale use. Therefore, the investigation of a comparable low-cost and abundant material is highly desirable. Consequently, many studies of the catalytic properties were performed in a short time; in particular, metal alloys, TMDs, phosphides, borides, and carbides were investigated [77]. Among those, TMD materials showed very promising catalytic properties to be exploited in HER cathodes [78]. Moreover, TMDs have been regarded as promising candidate catalysts because of their unique properties, such as the number of active sites and the basal surface, which arise from the 2D planar structures, and these properties enable a high catalytic performance in catalyzing HER [79]. For example, three factors help to fabricate more efficient and advantageous HER catalysts: 1) atomic-sized layered TMDs and a large surface area help to increase the number of active sites for a given number of total atoms, 2) the specific surface area allows these materials to serve as ideal platforms to

couple with other materials or substrates, and 3) their surface can be easily activated and optimized to obtain higher HER activity by regulating defects, strain and heteroatoms [56].

Although there are many advantages as mentioned above, some of the barriers still remain. The durability of HER electrocatalysts is still affected by inevitable corrosion during electrolysis; as a result, sturdy catalysts should be investigated further. Moreover, the HER mechanisms for 2D TMD thin films remain unclear and require further exploration. The properties of HER with 2DMs are shown in Table 4.

Table 4 Summary of properties of HER and OER with 2DMs.

Catalyst	Electrolyte	Current density [mA cm ⁻²]	Exchange current density [mA cm ⁻²]	Over-potential	Tafel slope [mV dec ⁻¹]	Ref
MoS ₂	0.5 M	10	0.6×10^{-4}		140	80
MoSe ₂	H ₂ SO ₄	10	3.8×10^{-4}	250	59.8	81
NiS _x	1 M KOH	10		372	41	82
ReS ₂				200	103	83
VS ₂	0.5 M	10	67.6×10^3	68	34	84
WSe ₂	H ₂ SO ₄	10		200	77.4	81
WTe ₂		10		0.35	57	85

Additionally, 2D TMDs are gaining significant attention as electrode materials for energy storage, such as in supercapacitors and Li-ion and Na-ion batteries. A battery is an electrochemical energy storage device that can reversibly convert chemical energy to electrical power. TMDs are promising catalytic materials because of their uniqueness arising from their physicochemical properties [86]. Recently, many reports about batteries based on TMDs to obtain high

performance have been published. One layer of TMD consists of three atom layers, in which one layer of metal atoms exists between two chalcogen layers, and each layer is bonded weakly by van der Waals forces, which helps to easily intercalate and deintercalate electrolyte ions from TMDs.

Regarding supercapacitors, 2D TMDs are the most promising candidates for supercapacitor electrodes because of their low weight and flexibility. At the same time, a high capacity, an excellent rate and cycling stability are simultaneously needed for future applications. The following points must be considered for the electrodes: 1) active materials have to be able to penetrate them; 2) to avoid aggregation of nanosheets and provide efficient ion transport pathways within the electrode, fabricating heterostructures and more complicated morphologies is essential; and 3) a theoretical study of the interfacial reaction between the electrode and electrolyte is also needed. The properties of supercapacitors with 2DMs are summarized in Table 5.

Table 5 Summary of the properties of supercapacitors with 2DMs.

Electrode materials	Areal capacitance [mF cm ⁻²]	Cycling stability	Ref
CoS ₂		94.4% after 2k cycles	87
MoS ₂	3400 @ Current density of 3 mA cm ⁻³	82% after 4.5k cycles	88
VS ₂		85% after 1k cycles	50
WS ₂	18.3 @ 5 mVs ⁻¹ scan rate	98% after 30k cycles	89

TMDs have aroused strong interest due to their crystal structures, excellent mechanical properties, and robust possibilities for many applications that have energy concerns. Accordingly, TMDs are regarded as promising anode materials in

the ion-battery field because of their large surface areas, and the interlayer spaces of TMDs provide locations to place Li⁺ ions, which results in relatively low operation voltage and energy density [90].

For energy storage devices, such as lithium ion batteries (LIBs), TMDs have been regarded as a strong candidate for high-efficiency energy storage as anode/cathode materials due to their atomically layered structure, high surface area, and outstanding electrochemical properties. Employing heterostructures is a prominent strategy for improving electron transportation and ion diffusion [91]. However, several downsides still remain and must be treated in the future: 1) determining the proper synthesis method to obtain a high volume-to-surface ratio is mandatory; 2) building a nanosized 3D structure is also necessary due to the poor conductivity; 3) because the correspondence between the structure and performance is not yet clear during the charge/discharge performance, a theoretical study is needed; and 4) safety issues exist [92]. The properties of lithium- /sodium-ion batteries with 2DMs are shown in Table 6.

Table 6 Summary of properties of lithium-/sodium-ion batteries with 2DMs.

Battery	Material	Charge/discharge capacity [mAh g ⁻¹]	Current density [mA g ⁻¹]	Cycles	Voltage window [V]	Ref
Li-ion	MnS	1205/1180	100	40	0.01-3	93
	MoS ₂	620/1040	4 × 10 ³	1000	0.005-3	94
	ReS ₂	750	732	300	1.5-2.8	83
	WS ₂	5.5 μAh cm ⁻²	50 μA cm ⁻²	10	0.1-2.5	95
Na-ion	MoS ₂	1710	0.5 ~ 4×10 ⁴	100	1-3	96
	WS ₂	356	200	2	0.001-3	97

2D layered TMD nanomaterials are considered to be promising alternatives for next-generation data storage devices because of their superior transparency, layered structural simplicity, and ability to stack into 3D structures following vdW heterostructures [98]. Recently, many studies that aim to fabricate TMDs as memory and logic devices have been conducted because easy and low-cost processes are important factors for developing nonvolatile memory on ultrathin 2DMs. Many studies eventually suggested that TMDs could be influential in finding the route to scaled-down and power-saving nonvolatile memory devices based on 2DM flash memories [99]. However, device engineering that improves device performance based on a precise understanding of the switching mechanism is needed. To achieve prominent device performances, for example, process engineering for the active channel and/or electrodes is a vital matter.

c. Magneto-thermoelectric properties of TMDs

Thermoelectric (TE) technology is regarded as an alternative and environmentally friendly technology for harvesting and recovering waste heat, which is directly converted into electrical energy using TE generators. The TE material generates electrical power from the heat energy, and reverse events can occur when we apply electrical power [100]. As the demand to reduce device size increases, 2D TMD materials have been highlighted due to their quantum confinement, resulting in an enhancement of the Seebeck coefficient. Additionally, many interfaces scatter phonons more effectively than electrons, and

preferentially scattering those phonons that contribute most to the thermal conductivity results in increased values of ZT , which is the dimensionless figure of merit [101]. This value can be expressed by the equation, $ZT = S^2\sigma T/k$, where S is the Seebeck coefficient, σ is the electrical conductivity, T is the absolute temperature, and k is the thermal conductivity. Despite the advantages mentioned above, the main disadvantage of TE cooling to be considered is its low energy efficiency. As a result, many studies have attempted to improve the thermoelectric properties. Thus, there are two primary approaches for improving the ZT of TE materials. The first concept involves the “phonon glass electron crystal,” proposing that an ideal TE material should have a form that combine glass-like thermal conductivity and crystal-like electronic properties [102]. Second, the ZT of TE materials can be enhanced by forming a nanostructure for which the density of states (DOS) near the Fermi level energy can be enhanced via quantum confinement, therefore increasing the Seebeck coefficient [101, 103].

Recently, the AHE in TMD materials has been verified. It is regarded as a potential material for spin-calorimetric devices [104]. Consequently, TMDs have attracted interest due to their fascinating electrical properties, such as photonic-induced AHE, valley Hall effect (VHE), and quantum Hall effect, to name a few [105, 106]. The ANE is a counterpart of the AHE and received increasing interest because the origin of both the AHE and ANE has contributions from extrinsic and intrinsic mechanisms [21]. However, regarding magneto-thermoelectric properties in TMDs, the publication density is very limited. In theoretical predictions, many studies anticipated the AHE and the ANE in these materials [107-109], but only a

few were experimentally tested. For example, several studies investigated the VHE in MoS₂ [110, 111]. In more detail, these studies produced one to several layers MoS₂ FET devices with a finite anomalous Hall voltage using a spin-dependent system by having illuminating polarized light. Similarly, the WX₂ (X= S, Se and Te) system has been studied in AHE and valleytronic associated fields [112, 113]. However, the interest in the magneto-thermoelectric character of TMDs has increased but experimental observations are limited [104, 114-116]. As a result, new investigations to verify the magneto-thermoelectric character are necessary.

5. Magneto-thermoelectrical properties in CoFeB thin film

a. Introduction

In the last chapter, we summarized many properties of TMDs and found a deficiency of studies of MTE properties. Now, we demonstrate a measurement platform to evaluate the MTE properties, and we tend to use similar investigations to examine the properties of ferromagnets: CoFeB. Ferromagnetic CoFeB has been studied widely and has been highlighted for applications in spintronics due to its high spin polarization [117]. Consequently, the CoFeB has been used in various spintronics devices such as magnetic tunnel junctions [118], spin valves [119], and spin-torque devices [120]. As the size of the device decreases due to commercial needs, a proper understanding of the thin-film is required. There are studies of thin films of CoFeB combined with other materials, more specifically $\text{Ir}_{22}\text{Mn}_{78}/\text{CoFeB}/\text{MgO}$ [121] and CoFeB/Pt [122] layers with perpendicular magnetic anisotropy and Py-covered [123] CoFeB nanotubes, which show AHE and ANE. Although $\text{Co}_{40}\text{Fe}_{40}\text{B}_{20}$ is regarded as a standard material that displays AHE and ANE, reports using only $\text{Co}_{40}\text{Fe}_{40}\text{B}_{20}$ thin films are limited. Accordingly, the study of the AHE and the ANE of pure $\text{Co}_{40}\text{Fe}_{40}\text{B}_{20}$ is necessary. Hence, in this chapter, we focused on $\text{Co}_{40}\text{Fe}_{40}\text{B}_{20}$ films alone to understand their nature.

b. Results and discussion

A $\text{Co}_{40}\text{Fe}_{40}\text{B}_{20}$ thin film with a thickness of 60 nm was grown on a Si/SiO₂ substrate. A Bestec magnetron sputtering system was used for the deposition of the films, with a single target of $\text{Co}_{40}\text{Fe}_{40}\text{B}_{20}$ as a source. Prior to deposition, the chamber was evacuated to a base pressure of less than 10^{-9} mbar, while the process gas (Ar 5 N) pressure was 3.5×10^{-3} mbar. The target was deposited by applying 30 W DC power and the total deposition rate was 0.1 Å/s. The substrate was rotated during deposition to ensure homogeneous growth.

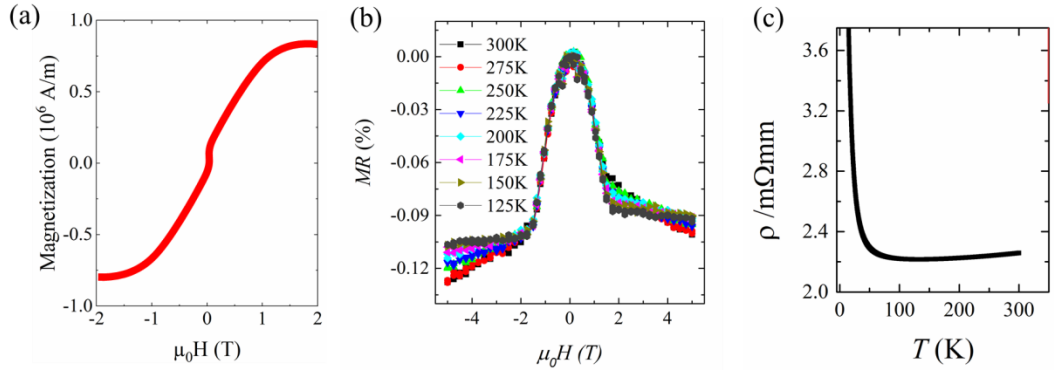


Fig. 12 (a) Magnetization of the $\text{Co}_{40}\text{Fe}_{40}\text{B}_{20}$ 60 nm film by SQUID magnetometry at 300 K. (b) Magnetoresistance (%) at various temperatures. (c) Longitudinal resistivity as a function of temperature. Reused Fig 1(a) in [125] by AIP publishing.

The magnetization of $\text{Co}_{40}\text{Fe}_{40}\text{B}_{20}$ was measured in a QD SQUID magnetometer. The results are shown in Fig. 12(a). A volume magnetization of ~ 800 kA/m at room temperature for the material is consistent with that of previous studies [125]. The magnetoresistance (MR) for each temperature shows similar behavior, as depicted in Fig. 12 (b). Furthermore, Fig. 12 (c) shows the longitudinal

resistivity as (ρ_{xy}) increases with decreasing temperature. As a consequence, 60 nm $\text{Co}_{40}\text{Fe}_{40}\text{B}_{20}$ shows typical ferromagnetic behavior, which correspond to previous studies [126].

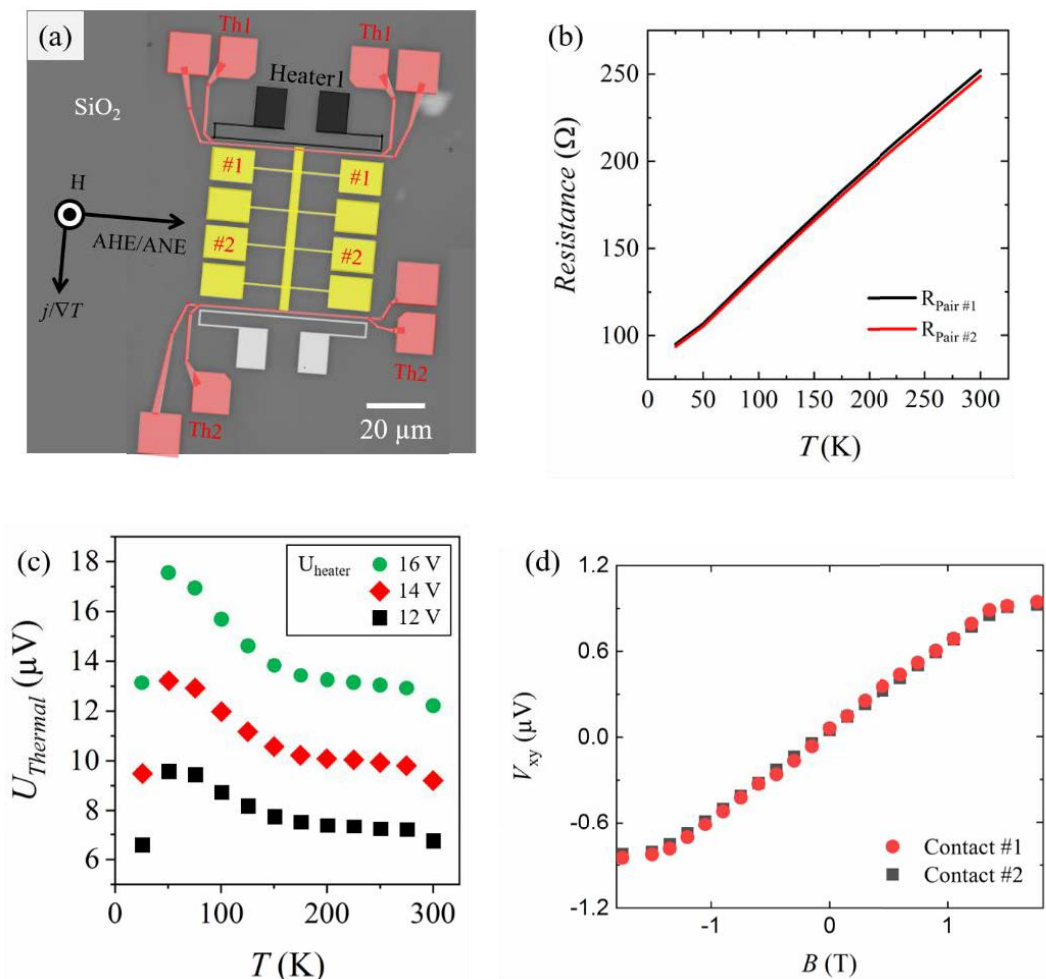


Fig. 13 Optical microscopy and thermal gradient evaluation. (a) Artificial color optical microscopy image of the $\text{Co}_{40}\text{Fe}_{40}\text{B}_{20}$ platform. (b) The calibration curves of Th1 and Th2 measured at the corresponding pairs during homogeneous heating of the sample. (c) The voltages measured at the two thermometers at different heater powers with various base temperatures. (d) Homogeneity of the thermal gradient measured at two pairs of contacts (#1 and #2).

The thin films were then patterned into Hall bars by optical lithography and plasma etching. After etching, the heater and thermometers were defined in a lift-off process with 30 nm Pt. A microscope image of the resulting whole structure is shown in Fig. 13 (a). The temperature gradient was generated by a heater and the temperature changes on each hot and cold part were monitored by two on-chip thermometers (Th1 and Th2). A perpendicular external magnetic field was applied to the sample plane. Transport measurements were performed in a cryostatic system (PPMS DynaCool from Quantum Design) equipped with a 9 T electromagnet. Additionally, the system is used to monitor the base temperature of the sample. Consequently, we evaluated the thermal gradient as $\nabla T = \Delta T / L$, where ΔT is the temperature difference, and L is the distance between the on-chip thermometers Th1 and Th2 (55 μm). In Fig. 13(b), the resistance at each thermometer as a function of the base temperature is measured, and the calibration curve can be used to evaluate the thermal gradient. The measured voltages from Th1 and Th2 cells at various temperatures are presented in Fig. 13 (c). During the process, the heater power is increased stepwise over each base temperature due to the thermal conductivity of the substrate (Si/SiO₂) and can be varied by changing the base temperature. Overall, we determined the ∇T of the thermal gradient evaluation. Notably, the two anomalous Nernst voltage values (V_{xy}) measured at the two pairs of contacts #1 and #2 in Fig. 13 (a) show negligible differences, indicating a homogenous thermal gradient in Fig. 13 (d).

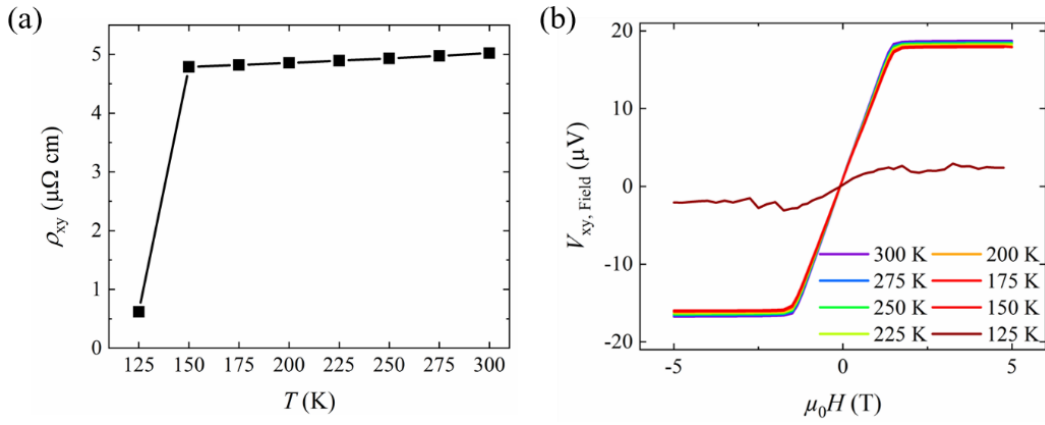


Fig. 14 Anomalous Hall measurement. (a) The anomalous Hall resistivity ρ_{xy} as a function of the temperature. (b) Field dependent anomalous Hall voltages.

The AHE evaluation was performed by using the structure depicted in Fig. 2(a) and the evaluated anomalous Hall resistivity ρ_{xy} with various temperature regimes is shown in Fig. 14 (a). Fig. 14(b) shows V_{xy} as a function of the applied external field $\mu_0 H$. The saturation field for most temperatures is 1.5 T. V_{xy} was approximately $17.27 \pm 0.02 \mu\text{V}$ with an average value above 150 K but significantly decreased to $2.16 \pm 0.23 \mu\text{V}$. Consequently, we observed a clear temperature dependency of the AHE sign and a significant decrease once the base temperature decreased to 125 K. This behavior corresponds to a previous study [127].

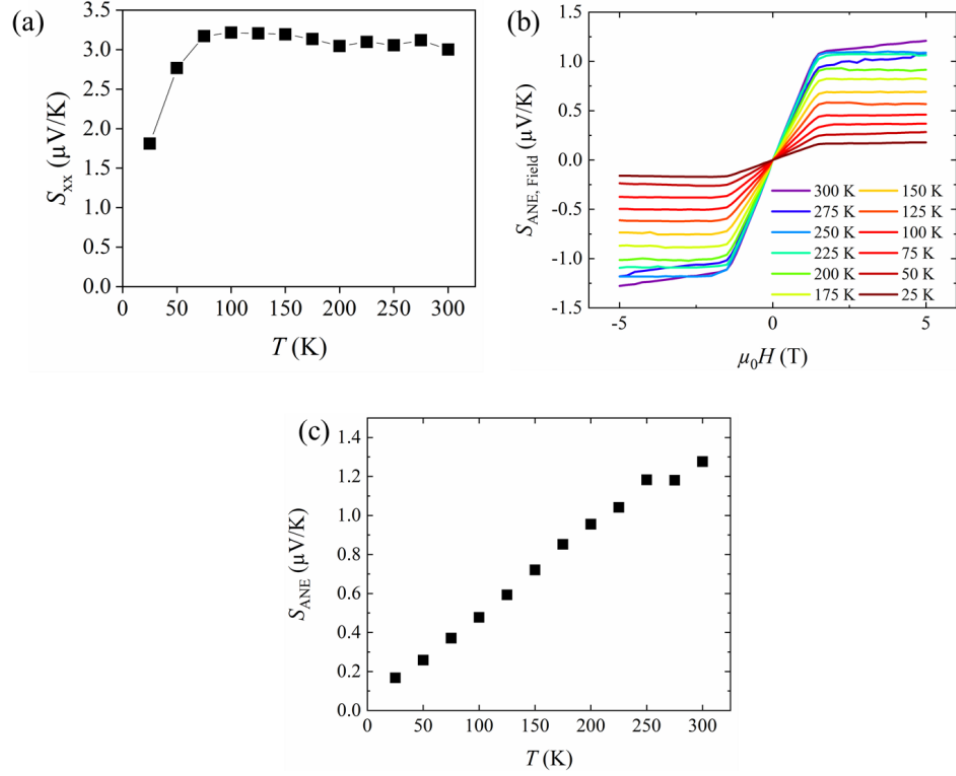


Fig. 15 Temperature dependence of (a) the Seebeck coefficient. (b) Field dependence of $S_{ANE,Field}$ with the external magnetic field variation. (c) Evaluated S_{ANE} of $\text{Co}_{40}\text{Fe}_{40}\text{B}_{20}$ thin films at various temperatures.

We evaluated the Seebeck coefficient as $S_{xx} = -V_{xx}/\nabla T$, where V_{xx} is the Seebeck voltage. As the temperature decreased to 50 K, the Seebeck coefficient decreased from 3 $\mu\text{V/K}$ to 1.8 $\mu\text{V/K}$, as shown in Fig. 15 (a). To quantify the ANE, we can determine the anomalous Nernst coefficient as S_{ANE} by $E_{ANE} = -S_{ANE}m \times \nabla T$, where E_{ANE} and m are the electric field induced by the ANE and the magnetization vector, respectively. The results of the ANE measurements for the magnetic field and temperature dependence are presented in Fig. 15 (b), (c), respectively. Before applying ∇T , the base temperature of the setup was determined at a specific temperature. Then, a current was applied to a heater to

generate a temperature gradient. Two thermometers were employed to quantify ∇T , afterwards, the S_{ANE} values were evaluated. In the measured temperature range from 25 K to 300 K, S_{ANE} gradually increased with increasing temperature, as shown in Fig 13 (c).

c. Conclusions

To conclude, we prepared an ultrathin film of $\text{Co}_{40}\text{Fe}_{40}\text{B}_{20}$ by magnetron sputtering. We systematically investigated the anomalous Hall and the anomalous Nernst effect in a $\text{Co}_{40}\text{Fe}_{40}\text{B}_{20}$ and confirmed the value above $-1 \mu\text{V/K}$ in the 60 nm thin film at room temperature. The evaluated anomalous Hall resistivity is $4.8 \sim 5 \mu\Omega \text{ cm}$ but decreases at 150 K to $0.48 \mu\Omega \text{ cm}$ due to the critical temperature. The Seebeck coefficient reached approximately $3.0 \mu\text{V/K}$ from 80 K. Finally, we systematically evaluated the thermoelectric and magnetotransport measurements of CoFeB thin films (60 nm) with our custom-made platform with various temperature regimes.

6. Anomalous Nernst and anomalous Hall effect in Co_2MnGa thin films

a. Introduction

In the last chapter, we examined the AHE and ANE of Co-Fe-B thin films. Now, we introduce similar investigations to look into the properties of a quantum material: Co_2MnGa . Co_2MnGa is a member of the Co_2YZ -based full Heusler family and has a high Curie temperature of 700 K and a high spin polarization [128]. Furthermore, Co_2MnGa has been highlighted because it is a magnetic Weyl semimetal and has an unconventional topological surface state [129-131]. Recently, the team of Belopolski systematically measured the anomalous Hall coefficient by considering the Berry curvature field and linked it with the evaluated topological Weyl fermion lines [132]. Additionally, recent work has identified the Berry curvature as the origin of the large AHE and suggested that the topology can be tuned by selecting the magnetic space group [11]. Experimentally, the magnetothermoelectric properties of bulk Co_2MnGa have found the anomalous Nernst coefficient (ANC or S_{xy}) of $-6 \mu\text{V}/\text{K}$ to be a top record [40].

The Mott relation can be applied in materials where each charge carrier acts independently [34, 133]. Furthermore, the Mott relation holds to account for the dominant intrinsic character in the anomalous transport in ferromagnetic materials such as the spinel feature of $\text{CuCr}_2\text{Se}_{4-x}\text{Br}_x$ [134], diluted magnetic semiconductors (DMS) [135], and with Berry phase or curvature [40, 136, 137]. However, recent theoretical work [136] suggests that the ANE could be sensitive to

electronic states invisible to the AHE and questions the validity of the Mott relation in materials with a nontrivial topology of the electronic bands. The relationship between the ANE and the AHE was systematically investigated by Pu *et al.* [135] in the ferromagnetic semiconductor GaMnAs, in which the AHE arises from the intrinsic spin-orbit coupling. A lack of systematic studies of the Mott relation in thin films with a nontrivial topology of the electronic states is arising from the fact that typically the ANE coefficient is small and not easy to measure and quantify. Additionally, a series of samples is required since a simple temperature dependent measurement of the nontrivial AHE and ANE in one sample is not conclusive.

In this study, we report a systematic study of the ANE in Co₂MnGa thin films that exhibit large S_{xy} values. We confirm the reported value of above $-2\mu\text{V/K}$ in the thickness range of 20 ~ 50 nm. We further employ the thickness series to study the relationship between the ANE and the AHE. We show the validity of the Mott relation in this particular material at 300 K by comparing the measured values of the anomalous Nernst conductivity with the calculated values.

b. Results and discussion

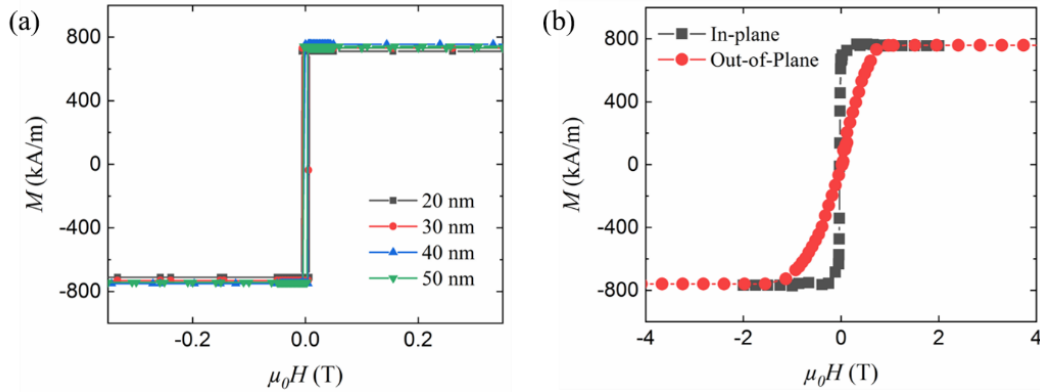


Fig. 16 (a) In-plane magnetization of Co_2MnGa thin films with thicknesses between 20 nm and 50 nm. All thicknesses exhibit a saturated magnetization of approximately 720 kA/m. (b) Comparison of in-plane and out-of-plane magnetization hysteresis loops of the 40 nm Co_2MnGa film measured at 300 K

Co_2MnGa thin films were deposited with various thicknesses (20, 30, 40 and 50 nm), by magnetron sputtering on MgO (001) substrates using a multisource Bestec UHV deposition system. As a capping layer to prevent oxidation, we deposited 3 nm of Al at room temperature. The thin films were post annealed at 500°C. The chemical composition and structural investigation conducted by X-ray techniques revealed Co_2MnGa Bragg peaks [138] revealing high degree of atomic order, consistent with previous work [124]. Unpatterned material was studied by SQUID magnetometry: All thicknesses exhibit saturated magnetization values of approximately 720 kA/m and similar coercive fields. Furthermore, we show typical in-plane and out-of-plane magnetization hysteresis loops for 20 ~ 50 nm Co_2MnGa films measured at 300 K in Fig. 16 (a) and (b).

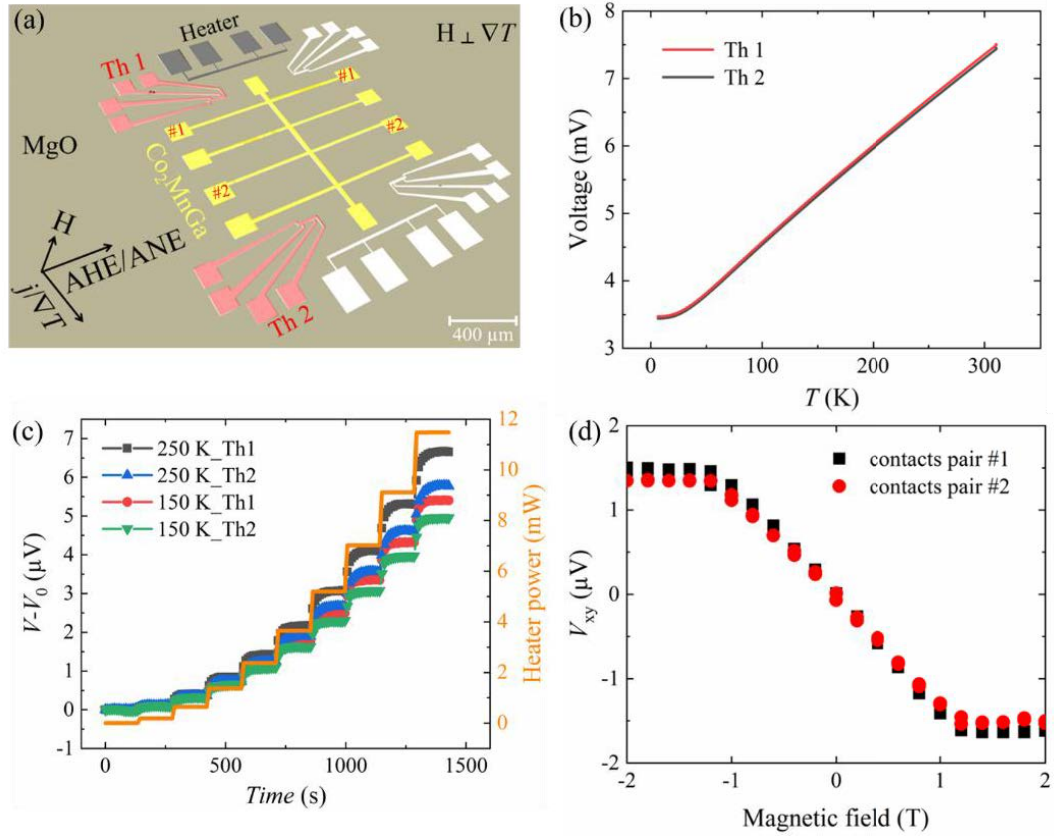


Fig. 17 Optical microscopy and thermal gradient evaluation. (a) False color optical microscopy image of our measurement platform. (b) The calibration curves of Th1 and Th2 measured at the corresponding pairs during homogeneous heating of the sample. (c) Voltages measured at the two thermometers at different heater power at two specific base temperatures of 150 K and 250 K. (d) Homogeneity of the thermal gradient measured at two pairs of contacts.

The films were defined to Hall bars by optical lithography and by etching. The Fig. 17 (a) shows the full devices structure. After etching, the heater and thermometers were defined in a lift-off process with 30 nm of deposited Pt. The temperature gradient was generated by an on-chip heater. The temperature on the cold and hot sides of the sample was monitored by on-chip thermometers (Th1 and Th2). An external magnetic field was applied perpendicular to the sample plane.

An Oxford Instruments cryostat with two thermometers is used to monitor the sample's base temperature. We determine the thermal gradient as $\nabla T = \Delta T / L$, where ΔT is the temperature difference and L is the distance between the on chip thermometers Th1 and Th2 (1.3 mm). In Fig. 17 (b), the measured voltage at each thermometer as a function of the base temperature is shown. We can evaluate the thermal gradient using a calibration curve. Fig. 17 (c) depicts the measured voltage from Th1 and Th2 at temperatures of 250 K and 150 K while the heater power is increased stepwise over time. We measured the same sequence at all temperatures because the thermal conductivity of MgO_x substrate can vary with the base temperature. Then, we evaluated ∇T to determine S_{xy} . Accordingly, we evaluated ∇T and the error of the thermal gradient evaluation. Note that the two anomalous Nernst voltage values (V_{xy}) measured at the two pairs of contacts #1 and #2 (Fig. 17 (a)) show only 7% difference indicating a homogenous thermal gradient in Fig. 17 (d). The thermal evaluation process is close to our previous work in Chap. 5, where we demonstrated that the thermal gradient along the y-direction is negligible [124, 139].

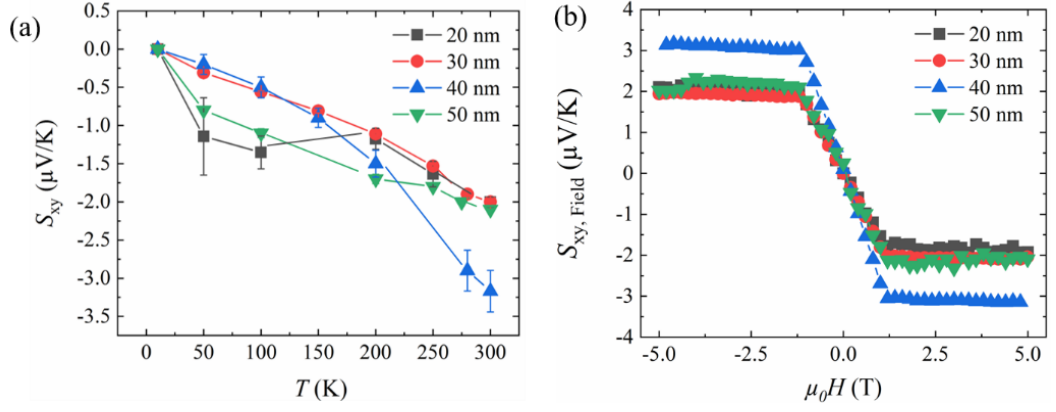


Fig. 18 Anomalous Nernst measurement. (a) Temperature dependence of S_{xy} evaluated for each sample thickness. (b) Magnetic field dependence of the $S_{xy,Field}$ at 300 K.

To evaluate S_{xy} , we swept the external magnetic field from -5 to 5 Tesla and quantified the S_{xy} at the transverse contacts #1. Notably, the difference of the measured value between contact #1 and #2 is rather trivial ($\sim 0.13 \mu\text{V/K}$). The ANC of all thicknesses of the Co_2MnGa thin films at various temperatures are presented in Fig. 18 (a). The ordinary Nernst effect is negligible compared to ANE in Co_2MnGa thin films. Consequently, $S_{xy,Field}$ at 300 K shows only a small change after saturation (Fig. 18 (b)). Therefore, the coefficient S_{xy} was evaluated in the following way: $E_{ANE} = -S_{xy}m \times \nabla T$, where E_{ANE} and m are the electric field induced by the ANE and the magnetization vector, respectively. Before applying temperature gradient as a function of distance as ∇T , the base temperature of the setup was obtained at a specific temperature. Then, a current was applied to a heater to generate a temperature gradient. Two thermometers were used to measure ∇T ,

afterwards, the S_{xy} values were quantified. In the measured temperature range from 10 K to 300 K, S_{xy} gradually increases with increasing temperatures, as expected for a magneto-thermal effect far below the Curie temperature (~ 700 K) [140]. All samples in the thickness range between 20 to 50 nm exhibits large S_{xy} above $-2 \mu\text{V/K}$. Among them, the 40 nm films exhibit even higher values of $-3 \mu\text{V/K}$.

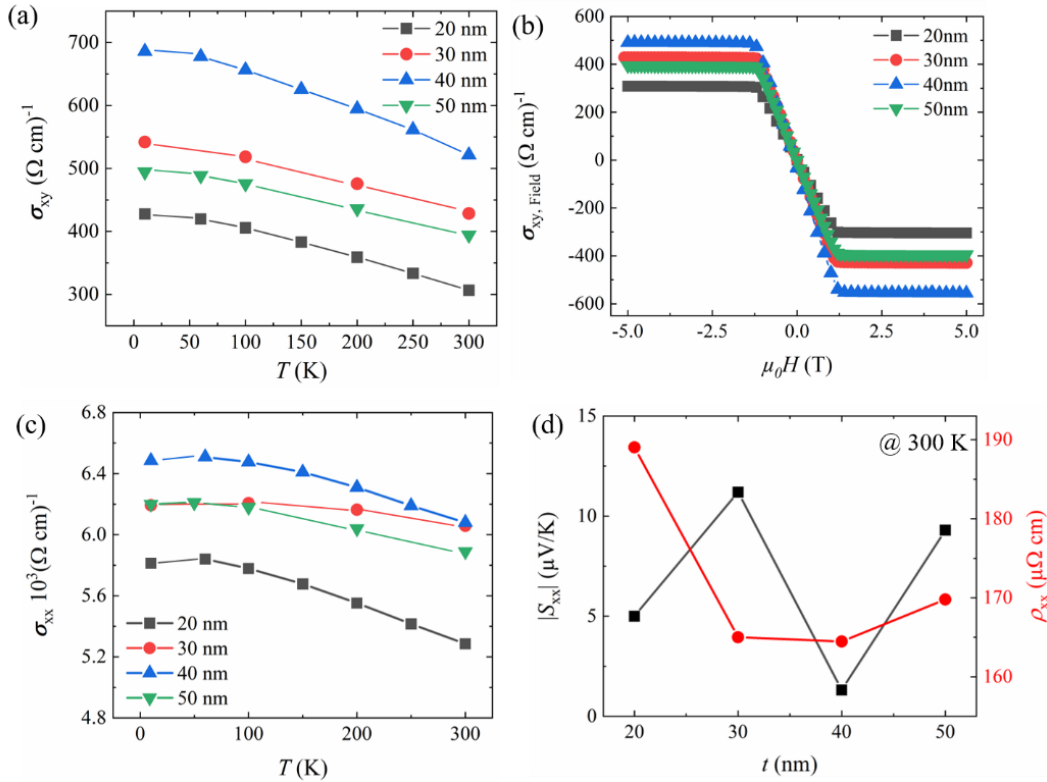


Fig. 19 (a) Temperature dependence of σ_{xy} evaluated for each sample thickness. (b) Magnetic field dependence of the $\sigma_{xy,Field}$ at 300 K. (c) Longitudinal conductivity σ_{xx} of each thickness as a function of temperature. (d) Thickness dependence of Seebeck coefficient S_{xx} and Longitudinal resistivity ρ_{xx} measured at 300 K.

Next, we evaluated the longitudinal conductivity as $\sigma_{xx} = 1/\rho_{xx}$ and the AHC as $\sigma_{xy} = -\rho_{xy}/(\rho_{xx}^2 + \rho_{xy}^2)$, where ρ_{xy} is the transversal and ρ_{xx} is the longitudinal resistivity [21, 39, 140]. The small decrease in σ_{xy} with increasing temperature is caused by the Hall resistivity slowly changing with the linear Hall coefficient as R_0 [11]. As a consequence, σ_{xy} gradually decreased with increasing temperature from 10 K to 300 K and shown in Fig. 19 (a). Fig. 19 (b) shows S_{xy} as a function of the applied external field $\mu_0 H$ at 300K. The ANE and the AHC are both weakly reduced in the 50 nm Co_2MnGa films, which could be related to the investigation reported in Ref. 131 and 141. For instance, Chuang *et al.* suggested that the intrinsic mechanism dominates at lower thicknesses. In this study, the ANE of Ni thin films increased to 25 nm and decreased at higher thicknesses, revealing that the enhancement of the ANE in thin films is mostly dominated by the intrinsic and side-jump mechanisms [142]. Furthermore, we note that thickness variations of the ANE cannot be explained by the variation in the magnetization, as shown in Fig. 16 (a). As shown already, the saturation magnetization of all measured samples is very similar. The longitudinal conductivity σ_{xx} is shown in Fig. 19 (c). In Fig. 19 (d), we evaluated the Seebeck coefficient (S_{xx}) using $S_{xx} = V_{xx}/\nabla T$, where V_{xx} is the Seebeck voltage at 300 K and measured the longitudinal resistivity ρ_{xx} . The variation of σ_{xx} and S_{xx} between various samples can be resulted from a weak stoichiometry variation, as shown for example by Sato *et al.* [143]. In Table I, we summarized the $|\sigma_{xx}|$, $|\sigma_{xy}|$, S_{xx} , $|\rho_{xx}|$, and $|\rho_{xy}|$ with thickness between 20 and 50 nm.

Table I. Summary of longitudinal and transversal resistivity and conductivity, and Seebeck coefficient measured at 300 K.

Thickness [nm]	$ \sigma_{xx} $ $10^3[\Omega \text{ cm}]^{-1}$	$ \sigma_{xy} $ $10^3[\Omega \text{ cm}]^{-1}$	S_{xx} [$\mu\text{V/K}$]	$ \rho_{xx} $ [$\mu\Omega \text{ cm}$]	$ \rho_{xy} $ [$\mu\Omega \text{ cm}$]
20	5.290	0.306	5.0	189.0	11.0
30	6.060	0.425	11.2	165.0	12.0
40	6.080	0.518	1.3	164.5	14.1
50	5.890	0.392	9.3	169.8	11.3

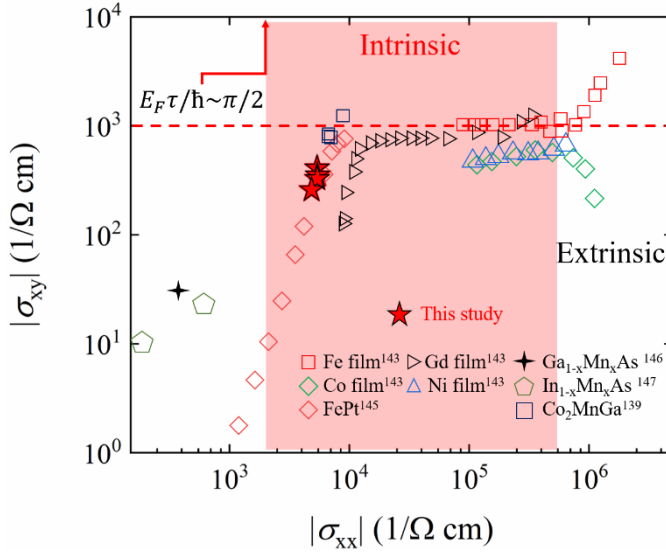


Fig. 20 Summary of the absolute values of σ_{xy} , as a function of σ_{xx} (determined experimentally) in various thin film materials. The data are taken from T. C. Chuang et al. (Ref. 142) for Fe, Gd, Co, and Ni thin film; from A. Markou et al. (Ref. 138) for Co_2MnGa ; from Y. M. Lu et al. (Ref. 144) for FePt; from K. W. Edmonds et al. (Ref. 145) for $\text{Ga}_{1-x}\text{Mn}_x\text{As}$; from A. Oiwa et al. (Ref. 146) for $\text{In}_{1-x}\text{Mn}_x\text{As}$.

In this part, we discuss the character of the AHE. Different contributions to the AHE can be studied by estimating the dependency between the longitudinal and transversal conductivity [39]. This approach was used to investigate many materials

in order to characterize intrinsic and extrinsic contributions to the AHE [147]. In the simplest scenario, three regions can be identified as illustrated in Fig. 20. First, in the poorly conducting regime ($\sigma_{xx} < \sim 3 \times 10^3 \Omega^{-1}cm^{-1}$), the dependence of σ_{xy} on the residual resistivity is well described by $\sigma_{xy}^{AHE} \propto \sigma_{xx}^{1.6}$ (experimentally) [147, 148]. Secondly, the behavior can be explained by the intrinsic Berry-phase contribution in the intermediate region ($\sigma_{xx} \sim 3 \times 10^3 - 5 \times 10^5 \Omega^{-1}cm^{-1}$) [149]. For our measurement of Co₂MnGa thin films, the combination of σ_{xx} and σ_{xy} is located in this region. Consequently, the AHE in Co₂MnGa thin films may include a Berry curvature contribution. Thirdly, in the extremely conducting case ($\sigma_{xx} \geq 5 \times 10^6 \Omega^{-1}cm^{-1}$), σ_{xy} depends on the constituents of the compounds and on Landau-level formation at low magnetic field due to the high mobility of the charge carriers [149].

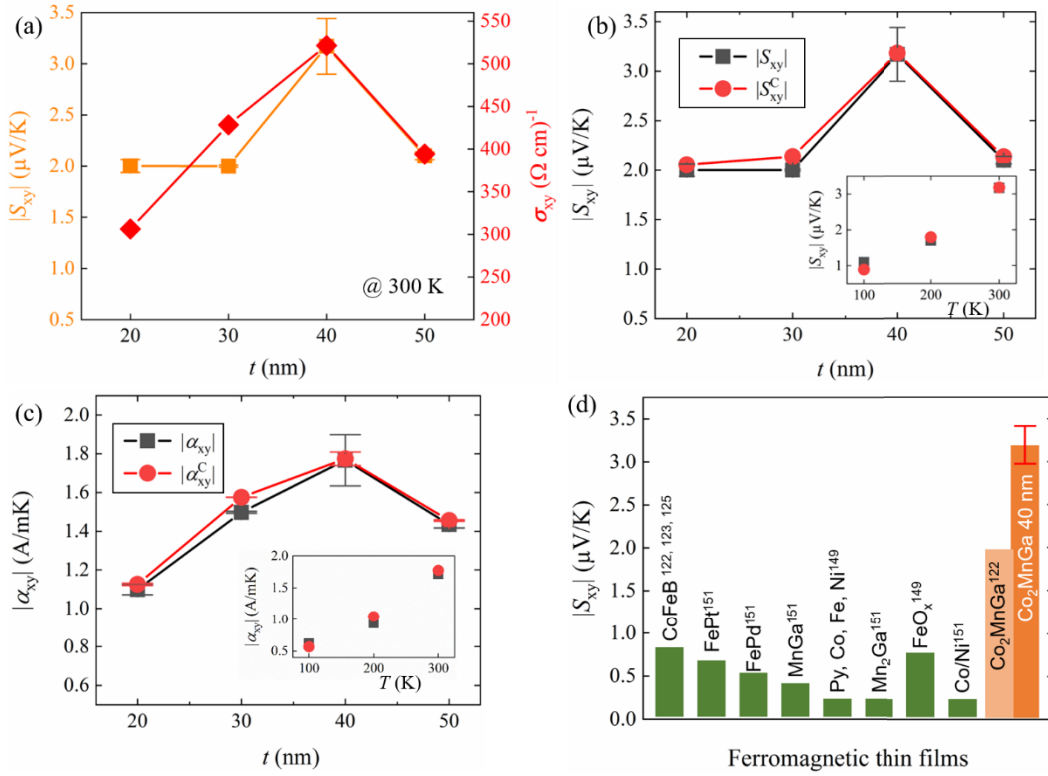


Fig. 21 (a) Thickness dependence of the ANE, the AHE, and Seebeck coefficient measured at 300 K. Measured and calculated thickness dependence of Nernst coefficient ($|S_{xy}|$ and $|S_{xy}^C|$) (b), and conductivity ($|\alpha_{xy}|$ and $|\alpha_{xy}^C|$), (c) for all samples at 300 K. The insets show the temperature dependence of $|S_{xy}|$ and $|\alpha_{xy}|$ in (b) and (c), respectively. Both insets depict the values for the 40 nm sample of Co_2MnGa . The calculated red circled symbols are the best fits using Eq. (1) and (2) with $n = 1.82 \pm 0.08$ for S_{xy}^C and $n = 1.86 \pm 0.05$ for α_{xy}^C , respectively. (d) Comparison of the $|S_{xy}|$ values of various ferromagnetic thin films and the current study at 300 K. The data are taken from H. Reichlova, J. Wells, and S. Tu et al. (Ref. 121, 122, 124) for Co_2FeB thin film; from T. C. Chuang et al. (Ref. 142) for Py, Co, Fe, and Ni thin film; from R. Ramos et al. (Ref. 148) for FeO_x thin film, from K. Hasegawa et al. (Ref. 150) for FePt, FePd, MnGa, Mn_2Ga , and Co/Ni thin film.

Our thickness series constitutes a good model system to investigate the Mott relation due to its large ANE. Additionally, the ANE presents an anomaly as a function of the thickness although the magnetization is identical for all studied

samples. Interestingly, most of the samples have similar ANE values of $\sim -2 \mu\text{V/K}$ (20, 30, and 50 nm), but one value is larger than the others, i.e. $\sim -3 \mu\text{V/K}$ (40 nm). These features are repeated in both the ANE and AHC measured at 300 K, as shown in Fig. 21 (a). Previous studies correlated the large ANE in Co_2MnGa with the intrinsic Berry curvature. Our studies, however, demonstrate that the ANE and AHE exhibit comparable trends in the full thickness range as can be seen in Fig. 21 (a) by direct comparison between the ANE and AHE. However, a more accurate test of the Mott relation needs knowledge of all four magneto-thermal transport coefficients and it will be presented in the following paragraphs. Finally, we provide a summary of the $|S_{xy}|$ values of various ferromagnetic thin films with thickness below $1 \mu\text{m}$ in Table II.

Table II. Overview of $|S_{xy}|$ values for various ferromagnetic thin films.

Material	$ S_{xy} $ [$\mu\text{V/K}$]	Thickness [nm]	Ref
CoFeB	0.8	15	121, 122, 124
FePt	0.65	30	150
FePd	0.5	30	150
Co/Ni	0.2	30	150
Mn_2Ga	0.2	30	150
$\text{L1}_0\text{-MnGa}$	0.2	30	150
FeO_x	0.74	50	148
Py, Co, Fe, Ni	0.06	1-100	142
Co_2MnGa	2	20, 50	124
Co_2MnGa	3.17 ± 0.27	40	This work

To get a more accurate test of the Mott relation, we employed an approach described by Guin and Pu *et al.* [40, 135]; because S_{xy} is related to the other

transport coefficients. As a consequence, we can calculate the transverse thermoelectric conductivity as $\alpha_{yx}(= -\alpha_{xy})$ by

$$\alpha_{yx} = \sigma_{yx}S_{xx} + \sigma_{xx}S_{yx} \quad (1)$$

where $S_{yx}(= -S_{xy})$. On the other hand, α_{xy} and S_{xy} can be calculated under the assumption that the Mott relation is valid. The measured values of perpendicular (ρ_{xx}), transversal resistivity (ρ_{xy}), and S_{xx} are employed to calculate $|S_{xy}^c|$ and $|\alpha_{xy}^c|$ as:

$$|S_{xy}^c| = \left| \frac{\rho_{xy}}{\rho_{xx}} \left(T \frac{\pi^2 k_B^2 \lambda'}{3e \lambda} - (n-1)S_{xx} \right) \right| \quad (2),$$

and

$$|\alpha_{xy}^c| = \left| \frac{\rho_{xy}}{\rho_{xx}^2} \left(T \frac{\pi^2 k_B^2 \lambda'}{3e \lambda} - (n-2)S_{xx} \right) \right| \quad (3)$$

Finally, we plotted calculated values together with the experimental values, such as $|S_{xy}|$ and $|\alpha_{xy}|$ in Fig. 21 (b) and (c). We can determine each pair of values for n and λ'/λ by fitting Eq. (2) to $|S_{xy}|$ [Fig. 21 (b)] or Eq. (3) to $|\alpha_{xy}|$ [Fig. 21 (c)] for all samples and temperatures. As a result, we evaluate $n = 1.82 \pm 0.08$, $\lambda'/\lambda = 3.25 \pm 0.05 \times 10^{19} J^{-1}$ for S_{xy}^c , $n = 1.86 \pm 0.05$, $\lambda'/\lambda = 3.25 \pm 0.0 \times 10^{19} J^{-1}$ for α_{xy}^c for all the presented data. These n values close to 2 correspond to a dominantly intrinsic character of the AHE. Furthermore, this leads to an excellent agreement between measured and calculated α_{xy}^c for the majority of thicknesses. This analysis reveals the applicability of

the Mott rule to the studied systems. Moreover, it shows the common physical origin behind the ANE and the AHE in the Weyl semimetal Co_2MnGa . In the end, we provide a summary of the $|S_{xy}|$, $|S_{xy}^C|$, $|a_{xy}|$, and $|a_{xy}^C|$ values of Co_2MnGa thin films with thickness series in Table III.

Table III. Summary of measured and calculated anomalous Nernst values and transverse thermoelectric conductivities at 300 K.

Thickness [nm]	$ S_{xy} $ [$\mu\text{V/K}$]	$ S_{xy}^C $ [$\mu\text{V/K}$]	$ a_{xy} $ [A/mK]	$ a_{xy}^C $ [A/mK]
20	2.00 ± 0.06	1.98 ± 0.08	1.21 ± 0.03	1.19 ± 0.02
30	2.00 ± 0.01	2.04 ± 0.16	1.69 ± 0.01	1.70 ± 0.05
40	3.17 ± 0.27	3.19 ± 0.10	2.00 ± 0.16	2.00 ± 0.01
50	2.10 ± 0.04	2.04 ± 0.13	1.60 ± 0.02	1.55 ± 0.04

Up to date, many studies have been made to search for the origin of the AHE and the ANE [11, 151]. High S_{xy} values were achieved by tuning band structure [40] and the chemical composition [152, 153] and were predicted in simulations [154]. These studies were not only motivated by the understanding of their consequences for magneto-thermal transport and the nature of the unconventional topological states, but were also motivated by a search for a path towards spin-caloritronic devices [122, 155]. To date, the source of this anomaly was explained by topological Weyl fermion lines in the Berry curvature in bulk systems [132]. On the other hand, extrinsic scattering effects are expected to be small in the thin film regime, because of the contributions from the surface states. Therefore, we can conclude it is justified to take the intrinsic contributions into account. Notably, this study provides a promising thin film material with a large S_{xy}

at 300 K, that is robust over a thickness range of 20 to 50 nm. We show various S_{xy} values for ferromagnetic thin films in Fig. 21 (d) for comparison. Therefore, it reveals that our Co_2MnGa thin films have outstanding S_{xy} values and represent a record value within the ferromagnetic thin film experiments at room temperature.

c. Summary

To summarize, we systematically investigated the anomalous Nernst effect in a thickness series of Co_2MnGa and confirmed the record large value above $-2 \mu\text{V/K}$ in the thickness range of 20 to 50 nm. Combining the electrical and the thermoelectric measurements and the extracted Nernst coefficients, we employed this system to study the Mott relation in thin films with a nontrivial topology inherent to band structure. We observed that the ANE is largest $-3 \mu\text{V/K}$ for the 40 nm thin film and found an analog trend when studying the AHE. By comparing various thicknesses with magnetometry measurements, we observe that this trend is independent of a variation of the magnetization. In agreement with recent reports, we believe that both the ANE and the AHC have contributions arising from not only finite Berry phase curvature. Moreover, in this thin film regime, intrinsic contributions play a dominant role. We show that the Mott relation is valid in this material with a nontrivial topology of the band structure.

7. Anomalous Hall effect in exfoliated VS₂ flakes

a. Introduction

In the previous chapter, we tested the AHE and the ANE of CoFeB and Co₂MnGa thin films. Finally, we present similar investigation to examine the properties of TMDs. Notably, TMD have attracted enormous interest because of their intriguing electrical transport properties, such as the valley Hall effect, charge density waves, and quantum Hall effect [104, 106, 156]. Material that have these properties have been regarded as strong candidates for spin-caloric devices and several valleytronic applications. However, if we compare 2D crystals to three-dimensional magnetic materials, the nature of the magnetism is recognizably different because the 2D area is more sensitive where quantum effect and wave function can play a critical role compared to 3D [115, 126]. Consequently, investigations of fundamental properties, such as the magnetotransport and thermoelectric properties, are important in 2D materials to understand their own nature.

However, experiments to characterize the magnetic properties of 2D crystals are challenging because the fabrication to make a suitable size and high-quality samples is demanding [41]. Furthermore, common tools for magnetization characterization, such as magnetometers, neutron scattering, and magnetic resonance techniques, often require a 3D bulk sample. As a result, we find a lack of studies of magnetic properties in 2D materials arising from the issues mentioned above.

VS₂, which is a member of the TMD materials, has very interesting properties and is used in applications in devices such as hydrogen evolution reactions (HERs) and field emission transistors (FETs) [41]. Additionally, it has been predicted by theoretical calculations that VS₂ possesses a unique quantum carrier transport character that could be used in quantum spintronics devices in the future [157]. In contrast to the relatively and experimentally well-explored properties, the analyses of the magnetotransport and thermoelectric properties in VS₂ are not well established. To date, there are many studies of the anomalous Hall resistivity contribution in transition metal dichalcogenides [106]. For example, Kang et al. reported the AHE in a few layers of WTe₂ and revealed the temperature dependence of the Hall conductivity results from both the intrinsic Berry curvature dipole and extrinsic spin-dependent scatterings [112]. Additionally, a theoretical calculation predicts the existence of Berry curvature in the VS₂ system [158].

In this work, we prepare VS₂ thin flakes by mechanical exfoliation from single crystals grown by the chemical vapor transport method. We use our custom-made platform to evaluate magnetotransports. Consequently, we study the temperature dependence of the magnetic properties in VS₂ nanoflakes. In this study, we confirm an AHE in the system. The temperature dependence of the MR and the AHE reveal a small shoulder and hump with 2.5 T to be external magnetic field below 20K.

b. Experiments

VS₂ powder was synthesized by a conventional solid-state reaction from the elements at 1073 K. Afterward, VS₂ single crystals were grown from VS₂

powder by means of chemical vapor transport reaction [159]. Three hundred milligrams of VS₂ powder and 10 mg of I₂ were placed in a silica tube. The tube was cooled in an LN₂ bath to prevent iodine evaporation and evacuated to 10⁻⁵ mbar. VS₂ single crystals were grown with a source temperature of 823 K and sink temperature of 773 K for one week [160]. The VS₂ samples could be further thinned down to 240 nm by peeling off by mechanical exfoliation methods onto a cleaned glass substrate. Standard optical lithography was employed to pattern the Hall bar structure and sputtered 5 nm Ti/150 nm Pt was used for evaluation. Transport measurements were performed in a cryostatic system (PPMS DynaCool from Quantum Design) equipped with a 9 T electromagnet with a temperature range of 2 K to 300 K.

c. Results and discussion

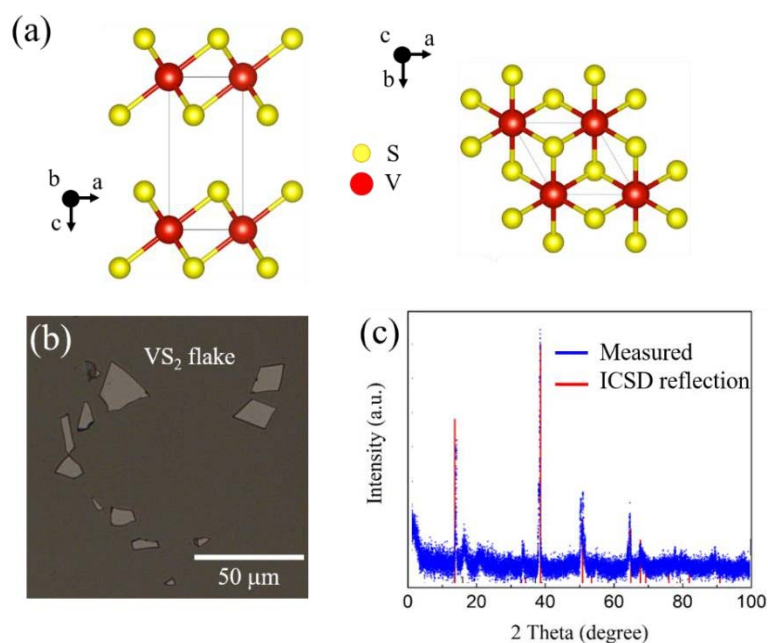


Fig. 22 (a) Side-view of the geometric structure of VS₂ left. The atomic structure of the VS₂ crystal projected along c-direction right. (b) An optical microscope image for VS₂ flakes. (c) X-ray diffraction pattern.

VS₂ has a CdI₂ structure type with the metal at 000 and chalcogen atoms at (1/3, 2/3, z) of the space group $P\bar{3}m1$ [160, 161], and the visualized structures are presented in Fig. 22 (a). An optical microscope (OM) image shows mechanically exfoliated VS₂ flakes by scotch tape in Fig. 22 (b). Structural information about VS₂ established by means of qualitative phase X-ray diffraction (PXRD) analysis in Fig. 22 (c). The main phase of the VS₂ sample was identified as VS₂ in the space group $P\bar{3}m1$.

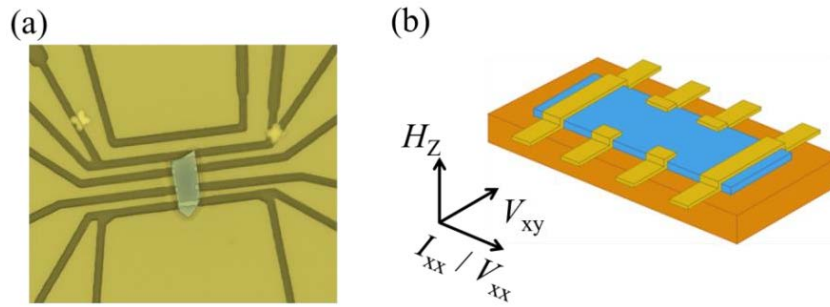


Fig. 23 (a) An optical image of a custom-made device with flake and Pt contact to measure electrical and magnetotransport properties.

(b) A schematic for the measurement.

Fig. 23 (a) shows an optical micrograph of the VS₂ device that was used to measure both longitudinal (V_{xx}) and transversal (V_{xy}) electrical transport properties. The devices were prepared by first exfoliating a VS₂ crystal and then transferring it to a glass substrate that was electrically insulating. These devices were used for electrical contacts to quantify resistivity based electrical properties from VS₂ flakes. All of these components of the device were fabricated from Pt films that were deposited on Ti seed layers (5 nm thickness). To measure V_{xx} and V_{xy} , a magnetic field is applied in the out of plane direction along the z-direction. A schematic of a typical device is shown in Fig. 21 (b).

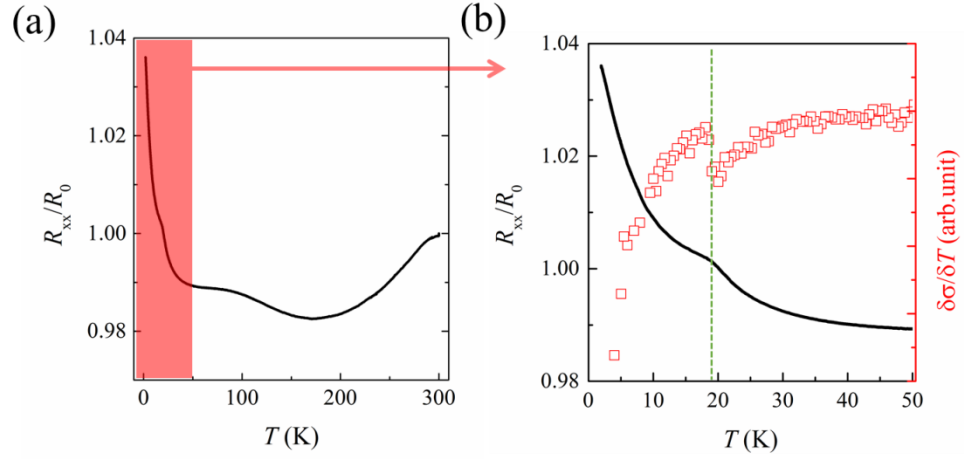


Fig. 24 (a) Normalized resistivity (ρ_{xx}/ρ_0) with various temperatures from 2 K to 300 K. (b) Reduced temperature range of (a) from 2 K to 50 K and calculated derivative as $d\rho/dT$.

We evaluated the longitudinal resistivity as $\rho_{xx} = V_{xx}/(I_{xx} \times d_{xx})$, where V_{xx} is the longitudinal voltage, I_{xx} is the applied current, and d_{xx} is the distance between the longitudinal contacts. The temperature dependence of the resistivity is shown in Fig. 24 (a). Notably, the resistivity is normalized to the 300 K resistivity value R_0 . The normalized resistivity to ρ_{300K} as ρ_0 (ρ_{xx}/ρ_0) is shown as metallic behavior between 20 ~ 300 K, and shows a kink at around 180 K in Fig. 24 (b), which may be due to the charged density wave [162]. In the lower temperature regime of approximately 20 K, a small deviation is found, which could occur when the magnetic phase transforms from paramagnetism (PM) to antiferromagnetism (AFM) in a V_5S_8 system [163]. However, in contrast to V_5S_8 , our system is VS_2 and this study shows that the 240 nm thin flake still has Curie temperature. More details, we will be in the discussion at the end of this part.

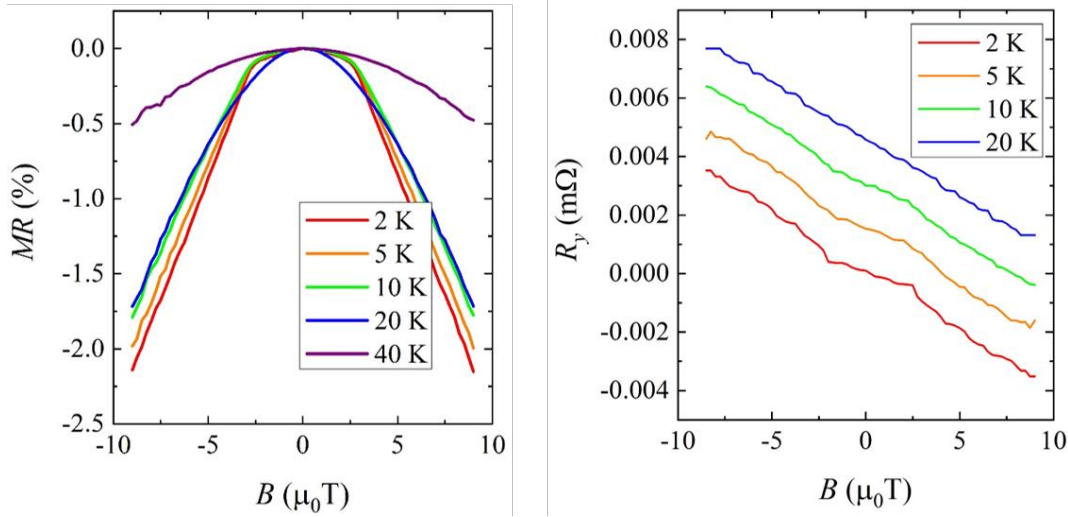


Fig. 25 (a) Magnetoresistance and (b) anomalous Hall resistance of a 240 nm VS_2 flake with various temperatures.

The MR of the VS_2 flake is measured under an out-of-plane magnetic field at different temperatures. The observed negative MR is shown in Fig. 25 (a). The MR has negative and parabolic behavior with a sudden decrease at 2.5 T before 20 K. There are several assumptions to understand this phenomenon. On the one hand, the spin flopping (SF) transition can contribute this when a magnetic field is applied to the c-axis with a critical field, i.e., $H_C \approx 2.5$ T [164]. On the other hand, the parabolic behavior can arise from Zeeman splitting holding with the Fukuyama model [165]. Additionally, the MR decreases with temperature and finally disappears at 20 K.

Fig. 25(b) shows the evaluated Hall resistance R_{yx} depicted with an external magnetic field from -9 T to 9 T at various temperatures. The trivial change in the slope of the Hall resistance are monitored at approximately 2.5 T and disappears

above 20 K. This finding can be attributed to either the two-band model [166] or interstitial defects of vanadium atoms within the van der Waals gaps, which can cause Anderson localization [167]. This defect can introduce magnetic moment changes into 2D systems or itinerant electrons, which can affect the magnetization [168]. While many studies have been conducted for a magnetic behavior in 2D systems [169], a study of magnetism in low-dimensional systems is necessary.

d. Summary

In summary, we investigated the electric transport properties of exfoliated VS_2 flakes at various temperatures. The longitudinal resistivity has two nontrivial kinks near 20 K and 100 K. We observed the negative and parabolic MR which may result from the Zeeman splitting effect with the Fukuyama model. Interestingly, we monitored an external magnetic field dependence at 2.5 T in MR and anomalous Hall resistance. In more detail, an obvious change in the slope of R_{yx} is observed at approximately 2.5 T. Two possible theories to understand this phenomenon are the two-band model and interstitial V atom generation at low temperature which can induce magnetization changes.

8. Summary

The final objective of this thesis was to investigate magneto-thermoelectric (MTE) properties in transition metal dichalcogenides (TMDs). Specifically, the aim of the research was to characterize and fabricate TMDs on the one hand, and the design of a measurement platform for the evaluation of MTE signals on the other hand. The following main points can be emphasized from the presented investigations:

1. For the state of the art in TMDs, we surveyed the recent progress in 2D TMD thin films and the current applications of these materials fabricated by chemical vapor deposition methods. Specifically, TMDs thin films have attracted much attention due to their unique magnetic, electrical, and optical properties. As a consequence, these materials have been widely used as favorable materials for optoelectronic, electronic transport and charge carrier devices. However, there is a lack of studies regarding MTE properties in TMDs, which is a fundamental characteristic in spin-caloritronic devices.

2. For $\text{Co}_{40}\text{Fe}_{40}\text{B}_{20}$, we evaluated the MTE properties in these thin films. The film has a typical thickness of 60 nm and was fabricated by physical vapor deposition. Additionally, we designed custom-made devices for MTE measurements, which fit thin films and resulted in an evaluation of not only the magnetoresistance and the Hall signal but also the magneto-thermoelectric properties in the same design. Consequently, this device can evaluate the thermal

gradient, and we found the Seebeck coefficient ($3 \mu\text{V/K}$), anomalous Hall voltages ($17 \mu\text{V}$), and anomalous Nernst coefficient ($1.2 \mu\text{V/K}$) at 300 K.

3. For Co_2MnGa , the design was applied to Co_2MnGa thin films to investigate the MTE properties. Additionally, we monitored the temperature and the thickness dependency of this material from 2 K to 300 K and from 20 to 50 nm, respectively. Moreover, we confirmed the record large ANE value of above $-3 \mu\text{V/K}$ and found a similar trend when studying the AHE. Combining the electrical and thermoelectric measurements and the evaluated Nernst coefficients, we employed this system to study the Mott relation in thin films. Furthermore, we found intrinsic contributions taking part as the dominant role in this thin film regime.

4. For TMD VS_2 , we tested similar investigations to examine the MTE properties of TMDs with a well-defined design. The VS_2 single crystals were grown by chemical vapor transport synthesis and mechanical exfoliation. The longitudinal resistivity has a kink at approximately 19 K. This kink can occur when the magnetic phase transforms from PM to AFM. Furthermore, we observed parabolic and negative MR. The MR has a distinct shoulder with an applied external magnetic field of 2.5 T, and it decreases steeply. Moreover, we defined an anomalous Hall effect at low temperatures that ranged from 20 K and monitored analogous magnetic response trends in MR. Subsequently, we traced this nontrivial temperature and external magnetic field dependency.

Acknowledgement

Reference

- [1] K. Behnia, The Nernst effect and the boundaries of the Fermi liquid picture, *Journal of Physics: Condensed Matter* 21, 113101 (2009).
- [2] T. Seebeck, Über die magnetische Polarisation der Metalle und Erze durch Temperaturdifferenz, *Ann. Phys.* 2(September), pp. 287–292, (1826).
- [3] C. Chien, *The Hall effect and its applications*, (Springer US, 2013).
- [4] E. M. Pugh, Hall effect and the magnetic properties of some ferromagnetic materials, *Phys. Rev.* 36, 1503-1511 (1930).
- [5] E. M. Pugh, T. W. Lippert, Hall emf and intensity of magnetization, *Phys. Rev.* 42, 709-713 (1932).
- [6] A. W. Smith, R. W. Sears, The Hall effect in Permalloy, *Phys. Rev.* 34, 1466-1473 (1929).
- [7] R. Karplus, J. M. Luttinger, Hall effect in ferromagnetics, *Phys. Rev.* 95, 1154-1160 (1954).
- [8] D. J. Thouless, M. Kohmoto, M. P. Nightingale, M. den Nijs, Quantized Hall conductance in a two-dimensional periodic potential, *Phys. Rev. Lett* 49, 405-408 (1982).
- [9] M. C. Chang, Q. Niu, Berry phase, hyperorbits, and the Hofstadter spectrum: Semiclassical dynamics in magnetic Bloch bands, *Phys. Rev. B* 53, 7010-7023 (1996).
- [10] G. Sundaram, Q. Niu, Wave-packet dynamics in slowly perturbed crystals: Gradient corrections and Berry-phase effects, *Phys. Rev. B* 59, 14915-14925 (1999).
- [11] K. Manna, L. Muechler, T. H. Kao, R. Stinshoff, Y. Zhang, J. Gooth, N. Kumar, G. Kreiner, K. Koepf, R. Car, J. Kuebler, G. H. Fecher, C. Shekhar, Y. Sun, C. Felser, From colossal to zero: controlling the anomalous Hall effect in magnetic Heusler compounds via Berry curvature design, *Phys. Rev. X* 8, 041045 (2018).
- [12] B. Bradlyn, L. Elcoro, J. Cano, M. G. Vergniory, Z. Wang, C. Felser, M. I. Aroyo, and B. A. Bernevig, Topological quantum chemistry, *Nature (London)* 547, 298 (2017).
- [13] H. Watanabe, H. C. Po, and A. Vishwanath, Structure and topology of band structures in the 1651 magnetic space groups, *Sci. Adv.* 4, eaat8685 (2018).

- [14] H. C. Po, A. Vishwanath, H. Watanabe, Symmetry-based indicators of band topology in the 230 space groups, *Nat. Commun.* 8, 50 (2017).
- [15] R. Shindou, N. Nagaosa, Orbital ferromagnetism and anomalous Hall effect in antiferromagnets on the distorted fcc lattice, *Phys. Rev. Lett.* 87, 116801 (2001).
- [16] H. Chen, Q. Niu, A. H. MacDonald, Anomalous Hall effect arising from noncollinear antiferromagnetism, *Phys. Rev. Lett.* 112, 017205 (2014).
- [17] J. Kübler, C. Felser, Non-Collinear Antiferromagnets and the Anomalous Hall Effect, *Europhys. Lett.* 108, 67001 (2014).
- [18] A. K. Nayak, J. E. Fischer, Y. Sun, B. Yan, J. Karel, A. C. Komarek, C. Shekhar, N. Kumar, W. Schnelle, J. Kuebler, C. Felser, S. S. P. Parkin, Large anomalous Hall effect driven by a nonvanishing Berry curvature in the noncolinear antiferromagnet Mn_3Ge , *Sci. Adv.* 2, e1501870 (2016).
- [19] S. Nakatsuji, N. Kiyohara, T. Higo, Large anomalous Hall effect in a non-collinear antiferromagnet at room temperature, *Nature (London)* 527, 212 (2015).
- [20] N. H. Sung, F. Ronning, J. D. Thompson, and E. D. Bauer, Comparing the anomalous Hall effect and the magneto-optical Kerr effect through antiferromagnetic phase transitions in Mn_3Sn , *Appl. Phys. Lett.* 112, 132406 (2018).
- [21] N. Nagaosa, J. Sinova, S. Onoda, A. H. MacDonald, N. P. Ong, Anomalous hall effect, *Rev. Mod. Phys.* 82, 1539 (2010).
- [22] D. Xiao, M.-C. Chang, Q. Niu, Berry phase effects on electronic properties, *Rev. Mod. Phys.* 82, 1959 (2010).
- [23] A. A. Burkov, Anomalous Hall effect in Weyl metals, *Phys. Rev. Lett.* 113, 187202 (2014).
- [24] J. Kübler, C. Felser, Weyl points in the ferromagnetic Heusler compound Co_2MnAl , *Europhys. Lett.* 114, 47005 (2016).
- [25] J. Kübler, C. Felser, Berry curvature and the anomalous Hall effect in Heusler compounds, *Phys. Rev. B* 85, 012405 (2012).
- [26] B. Bradlyn, J. Cano, Z. Wang, M. G. Vergniory, C. Felser, R. J. Cava, B. A. Bernevig, Beyond Dirac and Weyl fermions: Unconventional quasiparticles in conventional quasiparticles in conventional crystals, *Science* 353, aaf5037 (2016).
- [27] N. P. Armitage, E. J. Mele, A. Vishwanath, Weyl and Dirac semimetals in three-dimensional solids, *Rev. Mod. Phys.* 90, 015001 (2018).

- [28] K. Manna, Y. Sun, L. Muechler, J. Kübler, C. Felser, Heusler, Weyl and Berry, *Nat. Rev. Mater.* 3, 244 (2018).
- [29] T. Graf, C. Felser, S. S. Parkin, Simple rules for the understanding of Heusler compounds, *Prog. Solid State Chem.* 39, 1 (2011).
- [30] L. Wollmann, A. K. Nayak, S. S. Parkin, and C. Felser, Heusler 4.0: tunable materials, *Annu. Rev. Mater. Res.* 47, 247 (2017).
- [31] S. Sanvito, C. Oses, J. Xue, A. Tiwari, M. Zic, T. Archer, P. Tozman, M. Venkatesan, M. Coey, S. Curtarolo, Accelerated discovery of new magnets in the Heusler alloy family, *Sci. Adv.* 3, e1602241 (2017).
- [32] S. Chadov, T. Graf, K. Chadova, X. Dai, F. Casper, G. H. Fecher, C. Felser, Efficient spin injector scheme based on Heusler materials, *Phys. Rev. Lett.* 107, 0047202 (2011).
- [33] M. Cutler, N. Mott, Observation of Anderson localization in an electron gas, *Phys. Rev.* 181 (3): 1336 (1969).
- [34] N. F. Mott, H. Jones, The theory of the properties of metals and alloys, *Nature* 139, 348-349 (1937).
- [35] J. E. Mahan, *Physical Vapor Deposition of Thin Films*. Wiley-Interscience: 2000; p 336.
- [36] C. Muratore, J. J. Hu, B. Wang, M. A. Haque, J. E. Bultman, M. L. Jespersen, P. J. Shamberger, M. E. McConney, R. D. Naguy, A. A. Boevodin, Continuous ultra-thin MoS₂ films grown by low-temperature physical vapor deposition, *Appl. Phys. Lett.* 104, 261604 (2014).
- [37] A. K. Geim, K. S. Novoselov, The rise of graphene, *Nat. Mater.* 6, 183 (2007).
- [38] K. Geishendorf, R. Schlitz, P. Vir, C. Shekhar, C. Felser, K. Nielsch, S. T. B. Goennenwein, A. Thomas, Magnetoresistance and anomalous Hall effect in micro-ribbons of the magnetic Weyl semimetal Co₃Sn₂S₂, *Appl. Phys. Lett.* 114, 092403 (2019).
- [39] S. Onoda, N. Sugimoto, N. Nagaosa, Intrinsic versus extrinsic anomalous Hall effect in ferromagnets, *Phys. Rev. Lett.* 97, 126602 (2006).
- [40] S. N. Guin, K. Manna, J. Noky, S. J. Watzman, C. Fu, N. Kumar, W. Schnelle, C. Shekhar, Y. Sun, J. Gooth, C. Felser, Anomalous Nernst effect beyond the magnetization scaling relation in the ferromagnetic Heusler compound Co₂MnGa, *NPG Asia Mater.* 11, 16 (2019).

- [41] G. H. Park, K. Nielsch, A. Thomas, 2D transition metal dichalcogenide thin films obtained by chemical gas phase deposition techniques, *Adv. Mater. Interfaces.* 1800688 (2018).
- [42] S. Cho, S. Kim, J. H. Kim, J. Zhao, J. Seok, D. H. Keum, J. Baik, D. H. Choe, K. J. Chang, K. Suenaga, S. W. Kim, Y. H. Lee, H. Yang, Phase patterning for ohmic homojunction contact in MoTe₂, *Science* 349, 625 (2015).
- [43] Y. H. Lee, L. Yu, H. Wang, W. Fang, X. Ling, Y. Shi, C. T. Lin, J. K. Huang, M. T. Chang, C. S. Chang, M. Dresselhaus, T. Palacios, L. J. Li, J. Kong, Synthesis and transfer of single-layer transition metal disulfides on diverse surfaces, *Nano Lett.* 13, 1852-7 (2013).
- [44] Q. H. Wang, K. Kalantar-Zadeh, A. Kis, J. N. Coleman, M. S. Strano, Electronics and optoelectronics of two-dimensional transition metal dichalcogenides, *Nat. Nanotechnol.* 7, 699-712 (2012).
- [45] M. Amani, M. L. Chin, A. G. Birdwell, T. P. O'Regan, S. Najmaei, Z. Liu, P. M. Ajayan, J. Lou, M. Dubey, Electrical performance of monolayer MoS₂ field-effect transistors prepared by chemical vapor deposition, *Appl. Phys. Lett.* 102, 193107 (2013).
- [46] X. Wang, Y. Gong, G. Shi, W. L. Chow, K. Keyshar, G. Ye, R. Vajtai, J. Lou, Z. Liu, E. Ringe, B. K. Tay, P. M. Ajayan, Chemical vapor deposition growth of crystalline monolayer MoSe₂, *ACS Nano* 8, 5125-5131 (2014).
- [47] L. Zhou, K. Xu, A. Zubair, A. D. Liao, W. Fang, F. Ouyang, Y. H. Lee, K. Ueno, R. Saito, T. Palacios, J. Kong, M. S. Dresselhaus, Large area synthesis of high-quality uniform few-layer MoTe₂, *J. Am. Chem. Soc.* 137, 11892-11895 (2015).
- [48] H. Bark, Y. Choi, J. Jung, J. H. Kim, H. Kwon, J. Lee, Z. Lee, J. H. Cho, C. Lee, Large area niobium disulfide thin films as transparent electrodes for devices based on two-dimensional materials, *Nanoscale* 10, 1056-1062 (2018).
- [49] X. He, F. Liu, P. Hu, W. Fu, X. Wang, Q. Zeng, W. Zhao, Z. Liu, Chemical vapor deposition of high-quality and atomically layered ReS₂, *Small* 11, 5423-5429 (2015).
- [50] Q. Ji, C. Li, J. Wang, J. Niu, Y. Gong, Z. Zhang, Q. Fang, Y. Zhang, J. Shi, L. Liao, X. Wu, L. Gu, Z. Liu, Y. Zhang, Metallic Vanadium disulfide nanosheets as a platform for multifunctional electrode applications, *Nano. Lett.* 17, 4908-16 (2017).

- [51] K. Kang, S. Xie, L. Huang, Y. Han, P. Y. Huang, K. F. Mak, C. J. Kim, D. Muller, J. Park, High-mobility three-atom-thick semiconducting films with wafer-scale homogeneity, *Nature* 520, 656-660 (2015).
- [52] H. Zhou, C. Wang, J. C. Shaw, R. Cheng, Y. Chen, X. Huang, Y. Liu, N. O. Weiss, Z. Lin, Y. Huang, X. Duan, Large area growth and electrical properties of p-Type WSe₂ atomic layers, *Nano. Lett.* 15, 709-713 (2015).
- [53] E. Zhang, R. Chen, C. Huang, J. Yu, K. Zhang, W. Wang, S. Liu, J. Ling, X. Wan, H. Z. Lou, F. Xiu, Tunable positive to negative magnetoresistance in atomically thin WTe₂, *Nano. Lett.* 17, 878-885 (2017).
- [54] Y. Zhu, X. Wang, M. Zhang, C. Cai, L. Xie, Thickness and temperature dependent electrical properties of ZrS₂ thin films directly grown on hexagonal boron nitride, *Nano Res.*, 9, 2931-2937, (2016).
- [55] X. Yu, K. Sivula, Layered 2D semiconducting transition metal dichalcogenides for solar energy conversion, *Curr. Opin. Electrochem.* 2, 97-103 (2017).
- [56] Y. Chen, K. Yang, B. Jiang, J. Li, M. Zeng, L. Fu, Emerging two-dimensional nanomaterials for electrochemical hydrogen evolution, *J. Mater. Chem. A* 5, 8187-8208 (2017).
- [57] A. Splendiani, L. Sun, Y. Zhang, T. Li, J. Kim, C. Y. Chim, G. Gaill, F. Wang, Emerging photoluminescence in monolayer MoS₂, *Nano. Lett.* 10, 1271-1275 (2010).
- [58] L. Britnell, R. M. Ribeiro, A. Eckmann, R. Jalil, B. D. Belle, A. Mishchenko, Y. J. Kim, R. V. Gorbachev, T. Georgiou, Strong light-matter interactions in heterostructures of atomically thin film, *Science* 340, 1311-1314, (2013).
- [59] Y. Wang, Y. Bai, J. Xi, M. Liu, M. Li, K. Hong, Y. Sung, Continuous and large-area transition metal disulfides films deposited by pulsed laser/chemical vapor-combined process as a counter electrode for dye-sensitized solar cells, *Mater. Lett.* 201, 216-220 (2017).
- [60] J. Ma, H. Bai, W. Zhao, Y. Yuan, K. Zhang, High efficiency graphene/MoS₂/Si Schottky barrier solar cells using layer-controlled MoS₂ films, *Solar Energy* 160, 76-84 (2018).
- [61] S. Hussain, S. A. Patil, D. Vikraman, N. Mengal, H. Liu, W. Song, K. S. An, S. H. Jeong, H. S. Kim, J. Jung, Large area growth of MoTe₂ films as high performance counter electrodes for dye-sensitized solar cells, *Sci. Rep.* 8:29 (2018).

- [62] N. Mahuli, S. K. Sarkar, Atomic layer deposition of titanium sulfide and its application in extremely thin absorber solar cells, *J. Vac. Sci. Technol., A* 33, 01A150 (2015).
- [63] Y. Liu, N. O. Weiss, X. Duan, H. C. Cheng, Y. Huang, X. Duan, Van der Waals heterostructures and devices, *Nat. Rev. Mater.* 1, 16042 (2016).
- [64] J. Kim, H. Kim, W. J. Kim, Single layered MoS₂_PEI-PEG nanocomposite-mediated gene delivery controlled by photo and redox stimuli, *Small* 12, 1184 (2016).
- [65] O. V. Yazyev, A. Kis, MoS₂ and semiconductors in the flatland, *Mater. Today* 18, 20 (2015).
- [66] H. L. Liu, C. C. Shen, S. H. Su, C. L. Hsu, M. Y. Li, L. J. Li, Optical properties of monolayer transition metal dichalcogenides probed by spectroscopic ellipsometry, *Appl. Phys. Lett.* 105, 201905 (2014).
- [67] M. Ye, D. Zhang, Y. K. Yap, Recent advances in electronic and optoelectronic devices based on two-dimensional transition metal dichalcogenides, *Electronics* 6, 43 (2017).
- [68] D. Wang, X. Zhang, H. Liu, J. Meng, J. Xia, Z. Yin, Y. Wang, J. You, X. M. Meng, Epitaxial growth of HfS₂ on sapphire by chemical vapor deposition and application for photodetectors, *2D Mater.* 4, 031012 (2017).
- [69] C. Nie, L. Yu, X. Wei, J. Shen, W. Lu, W. Chen, S. Feng, H. Shi, Ultrafast growth of large-area monolayer MoS₂ film via gold foil assistant CVD for a highly sensitive photodetector, *Nanotechnology* 28, 275203 (2017).
- [70] D. D. Fazio, I. Goykhman, D. Yoon, M. Bruna, A. Eiden, S. Milana, U. Sassi, M. Barbone, D. Dumcenco, K. Marinov, A. Kis, High Responsivity, Large-Area Graphene/MoS₂ Flexible Photodetectors, *ACS Nano* 10, 9, 8252 (2016).
- [71] M. Hafeez, L. Gan, H. Li, Y. Ma, T. Zhai, Large-area bilayer ReS₂ film/multilayer ReS₂ flakes synthesized by chemical vapor deposition for high performance photodetectors, *Adv. Funct. Mater.* 26, 4551 (2016).
- [72] M. Hafeez, L. Gan, H. Lim, Y. Ma, T. Zhai, Chemical vapor deposition synthesis of ultrathin hexagonal ReSe₂ flakes for anisotropic Raman property and optoelectronic application, *Adv. Mater.* 28, 8296 (2016).
- [73] C. Lan, C. Li, Y. Yin, Y. Liu, Large-area synthesis of monolayer WS₂ and its ambient-sensitive photodetecting performance, *Nanoscale* 7, 5974 (2015).

- [74] J. Chen, B. Liu, Y. Liu, W. Tang, C. T. Nai, L. Li, J. Zheng, L. Gao, Y. Zheng, H. S. Shin, H. Y. Jeong, K. P. Loh, Chemical vapor deposition of large-sized hexagonal WSe₂ crystals on dielectric substrates, *Adv. Mater.* 27, 6722-6727 (2015).
- [75] X. Wang, L. Huang, X. W. Jiang, Y. Li, Z. Wei, J. Li, Large scale ZrS₂ atomically thin layers, *J. Mater. Chem. C* 4, 3143 (2016).
- [76] M. Chhowalla, H. S. Shin, G. Eda, L. J. Li, K. P. Loh, H. Zhang, The chemistry of two-dimensional layered transition metal dichalcogenide nanosheets, *Nat. Chem.* 5, 263-275 (2013).
- [77] M. Caban-Acevedo, M. L. Stone, J. R. Schmidt, J. G. Thomas, Q. Ding, H. C. Chang, M. L. Tsai, J. H. He, S. Jin, Efficient hydrogen evolution catalysis using ternary pyrite-type cobalt phosphosulphide, *Nat. Mater.* 14, 1245 (2015).
- [78] X. Cao, C. Tan, X. Zhang, W. Zhao, H. Zhang, Solution-processed two-dimensional metal dichalcogenide based nanomaterials for energy storage and conversion, *Adv. Mater.* 28, 6167 (2016).
- [79] H. Yin, Z. Tang, Ultrathin two-dimensional layered metal hydroxides: an emerging platform for advanced catalysis, energy conversion and storage, *Chem. Soc. Rev.* 45, 4873 (2016).
- [80] Y. Yu, S. Y. Huang, Y. Li, S. N. Steinmann, W. Yang, L. Cao, Layer dependent electrocatalysis of MoS₂ for Hydrogen evolution, *Nano Lett.* 14, 553 (2014).
- [81] H. Wang, D. Kong, P. Johannes, J. J. Cha, G. Zheng, K. Yan, N. Liu, Y. Cui, MoSe₂ and WSe₂ nanofilms with vertically aligned molecular layers on curved and rough surfaces, *Nano Lett.* 13, 3426 (2013).
- [82] H. Li, Y. Shao, Y. Su, Y. Gao, X. Wang, Vapor-phase atomic layer deposition of nickel sulfide and its application for efficient oxygen-evolution electrocatalysis, *Chem. Mater.* 28, 1155 (2016).
- [83] J. Gao, L. Li, J. Tan, H. Sun, B. Li, J. C. Idrobo, C. V. Singh, T. M. Lu, N. Koratkar, Vertically oriented arrays of ReS₂ nanosheets for electrochemical energy storage and electrocatalysis, *Nano Lett.* 16, 3780 (2016).
- [84] J. Yuan, J. Wu, W. J. Hardy, P. Loya, M. Lou, Y. Yang, S. Najmaei, M. Jian, F. Qin, K. Keyshar, H. Ji, W. Gao, J. Bao, J. Kono, D. Natelson, P. M. Ajayan, J. Lou, Facile synthesis of single crystal vanadium disulfide nanosheets by chemical vapor deposition for efficient hydrogen evolution reaction, *Adv. Mater.* 27, 5605 (2015).

- [85] J. Li, M. Hong, L. Sun, W. Zhang, H. Shu, H. Chang, Enhanced electrocatalytic hydrogen evolution from large-scale, facile-prepared, highly crystalline WTe₂ nanoribbons with Weyl semimetallic phase, *ACS Appl. Mater. Interfaces* 10, 458 (2018).
- [86] G. Cunningham, M. Lotya, C. S. Cucinotta, S. Sanvito, S. D. Bergin, R. Menzel, M. S. P. Shaffer, J. N. Coleman, Solvent exfoliation of transition metal dichalcogenides: dispersibility of exfoliated nanosheets varies only weakly between compounds, *ACS Nano* 6, 3468 (2012).
- [87] H. Li, Y. Gao, Y. Shao, Y. Su, X. Wang, Vapor phase atomic layer deposition of Co₉S₈ and its application for supercapacitor, *Nano Lett.* 15, 6689-6695 (2015).
- [88] D. K. Nandi, S. Sahoo, S. Sinha, S. Yeo, H. Kim, R. N. Bulakhe, J. Heo, J. J. Shim, S. H. Kim, Highly uniform atomic layer deposited MoS₂@3D Ni foam: a novel approach to prepare an electrode for supercapacitors, *ACS Appl. Mater. Interfaces* 9, 40252 (2017).
- [89] N. Choudhary, C. Li, H. S. Chung, J. Moore, J. Thomas, Y. Jung, High performance one-body core/shell nanowire supercapacitor enabled by conformal growth of capacitive 2D WS₂ layers, *ACS Nano* 10, 10726 (2016).
- [90] L. Shi, T. Zhao, Recent advances in inorganic 2D materials and their applications in lithium and sodium batteries, *J. Mater. Chem. A* 5, 3735 (2017).
- [91] X. Xie, T. Makaryan, M. Zhao, K. L. V. Aken, Y. Gogotsi, G. Wang, MoS₂ nanosheets vertically aligned on carbon paper: a freestanding electrode for highly reversible sodium-ion batteries, *Adv. Energy Mater.* 6, 1502161 (2016).
- [92] S. Wu, Y. Du, S. Sun, Transition metal dichalcogenide based nanomaterials for rechargeable batteries, *Chem. Eng. J.* 307, 189 (2017).
- [93] S. C. Riha, A. A. Koegel, X. Meng, I. S. Kim, Y. Cao, M. J. Pellin, J. W. Elam, A. B. F. Martinson, Atomic layer deposition of MnS: phase control and electrochemical applications, *ACS Appl. Mater. Interfaces* 8, 2774 (2016).
- [94] J. He, C. Zhang, H. Du, S. Zhang, P. Hu, Z. Zhang, Y. Ma, C. Huang, G. Cui, Engineering vertical aligned MoS₂ on graphene sheet towards thin film lithium ion battery, *Electrochim. Acta* 178, 476 (2015).
- [95] D. K. Nandi, U. K. Sen, S. Sinha, A. Dhara, S. Mitra, S. K. Sarkar, Atomic layer deposited tungsten nitride thin films as a new lithium-ion battery anode, *Phys. Chem. Chem. Phys.* 17, 17445 (2015).

- [96] M. B. Sreedhara, S. Gope, B. Vishal, R. Datta, A. J. Bhattacharyya, C. N. R. Rao, Atomic layer deposition of crystalline epitaxial MoS₂ nanowall networks exhibiting superior performance in thin-film rechargeable N-ion batteries, *J. Mater. Chem. A* 6, 2302 (2018).
- [97] S. H. Choi, Y. C. Kang, Sodium ion storage properties of WS₂-decorated three-dimensional reduced graphene oxide microspheres, *Nanoscale* 7, 3965 (2015).
- [98] A. K. Geim, I. V. Grigorieva, Van der Waals heterostructures, *Nature* 499, 419 (2013).
- [99] Q. A. Vu, H. Kim, V. L. Nguyen, U. Y. Won, S. Adhikari, K. Kim, Y. H. Lee, W. J. Yu, High on-off ratio floating gate memristor array on a flexible substrate via CVD-grown large-area 2D layer stacking, *Adv. Mater.* 29, 1703363 (2017).
- [100] K. Nielsch, J. Bachmann, J. Kimling, H. Böttner, Thermoelectric nanostructures: from physical model systems towards nanograined composites, *Adv. Energy Mater.* 1, 713 (2011).
- [101] M. S. Dresselhaus, G. Chen, M. Y. Tang, R. Yang, H. Lee, D. Wang, Z. Ren, J. P. Fleurial, P. Gogna, New directions for low-dimensional thermoelectric materials, *Adv. Mater.* 19, 1043 (2007).
- [102] M. H. Elsheikh, D. A. Shnawah, M. F. M. Sabri, S. B. M. Said, M. H. Hassan, M. A. Bashir, M. Mohamad, A review on thermoelectric renewable energy: principle parameters that affect their performance, *Renewable Sustainable Energy Rev.* 30, 337 (2014).
- [103] J. Mao, Z. Liu, Z. Ren, Size effect in thermoelectric materials, *npj Quantum Mater.* 1, 16028 (2016).
- [104] M. T. Dau, C. Vergnaud, A. Marty, C. Beigne, S. Gambarelli, V. Maurel, T. Journot, B. Hyot, T. Guillet, B. Grevin, H. Okuno, M. Jamet, The valley Nernst effect in WSe₂, *Nat. Comm.* 10, 5796 (2019).
- [105] N. Ubrig, S. Jo, M. Philippi, D. Costanzo, H. Berger, A. B. Kuzmenko, A. F. Morpurgo, Microscopic origin of the valley hall effect in transition metal dichalcogenides revealed by wavelength-dependent mapping, *Nano Lett.*, 17, 5719-5725 (2017).
- [106] S. Galeski, X. Zhao, R. Wawrzynczak, T. Meng, T. Förster, P. M. Lozano, S. Honnali, N. Lamba, T. Ehmcke, A. Markou, Q. Li, G. Gu, W. Zhu, J. Wosnitza, C. Felser, G. F. Chen, J. Gooth, Unconventional hall response in the quantum limit of HfTe₅, *Nat. Communications* 11, 5926 (2020).

- [107] X. Q. Yu, Z. G. Zhu, J. S. You, T. Low, G. Su, Topological nonlinear anomalous Nernst effect in strained transition metal dichalcogenides, *Phys. Rev. B* 99, 201410(R) (2019).
- [108] S. Konabe, T. Yamamoto, Valley photothermoelectric effects in transition-metal dichalcogenides, *Phys. Rev. B* 90, 075430 (2014).
- [109] G. Sharma, Tunable topological Nernst effect in two-dimensional transition metal dichalcogenides, *Phys. Rev. B* 98, 075416 (2018).
- [110] K. F. Mak, K. L. McGill, J. Park, P. L. McEuen, The valley hall effect in MoS₂ transistors, *Science* 27, 1489-1492 (2014).
- [111] J. Lee, K. F. Mak, J. Shan, Electrical control of the valley hall effect in bilayer MoS₂ transistors, *Nature Nanotechnology*, 11 421 (2016).
- [112] K. Kang, T. Li, E. Sohn, J. Shan, K. F. Mak, Nonlinear anomalous Hall effect in few-layer WTe₂, *Nature Mater.* 18 324-328 (2019).
- [113] H. Guan, N. Tang, H. Huang, X. Zhang, M. Su, X. Liu, L. Liao, W. Ge, B. Shen, Inversion symmetry breaking induced valley hall effect in multilayer WSe₂, *ACS Nano* 13, 9325-9331 (2019).
- [114] K. G. Rana, F. K. Dejene, N. Kumar, C. R. Rajamathi, K. Sklarek, C. Felser, S. S. P. Parkin, Thermopower and unconventional Nernst effect in the predicted type-II Weyl semimetal WTe₂, *Nano Lett.* 18, 6591-6596 (2018).
- [115] K. Hippalgaonkar, Y. Wang, Y. Ye, D. Y. Qiu, H. Zhu, Y. Wang, J. Moore, S. G. Louie, X. Zhang, High thermoelectric power factor in two-dimensional crystals of MoS₂, *Phys. Rev. B* 95, 115407 (2017).
- [116] J. Wu, H. Schmidt, K. K. Amara, X. Xu, G. Eda, B. Oezylmaz, Large thermoelectricity via variable range hopping in chemical vapor deposition grown single-layer MoS₂, *Nano Lett.* 14, 2730-2734 (2014).
- [117] S. X. Huang, T. Y. Chen, C. L. Chien, Spin polarization of amorphous CoFeB determined by point-contact Andreev reflection, *Appl. Phys. Lett.* 92, 242509 (2008).
- [118] W. G. Wang, C. Ni, G. X. Miao, C. Weiland, L. R. Shah, X. Fan, P. Parson, J. Jordan-weet, X. M. Kou, Y. P. Zhang, R. Strearrett, E. R. Nowak, R. Opila, J. S. Moodera, J. Q. Xiao, Understanding tunneling magnetoresistance during thermal annealing in MgO-based junctions with CoFeB electrodes, *Phys. Rev. B* 81, 144406 (2010).

- [119] C. Y. You, H. S. Goripati, T. Furubayashi, Y. K. Takahashi, K. Hono, Exchange bias of spin valve structure with a top-pinned $\text{Co}_{40}\text{Fe}_{40}\text{B}_{20}/\text{IrMn}$, *Appl. Phys. Lett.* 93, 012501 (2008).
- [120] A. A. Tulapurkar, Y. Suzuki, A. Fukushima, H. Kubota, H. Maehara, K. Tsunekawa, D. D. Djayaprawira, N. Watanabe, S. Yuasa, Spin torque diode effect in magnetic tunnel junctions, *Nature*, 438, 339-342 (2005).
- [121] S. Tu, J. Hu, G. Yu, H. Yu, C. Liu, F. Heimbach, X. Wang, J. Zhang, Y. Zhang A. Hamzic, Anomalous Nernst effect in $\text{Ir}_{22}\text{Mn}_{78}/\text{Co}_{20}\text{Fe}_{60}\text{B}_{20}/\text{MgO}$ layers with perpendicular magnetic anisotropy, *Appl. Phys. Lett.* 111, 222401 (2017).
- [122] J. Wells, E. Selezneva, P. Krzysteczko, X. Hu, H.W. Schumacher, R. Mansell, R. Cowburn, A. Cuenat and O. Kazakova, Combined anomalous Nernst effect and thermography studies of ultrathin CoFeB/Pt nanowires, *AIP Adv.* 7, 055904 (2017).
- [123] K. Baumgaertl, F. Heimbach, S. Maendl, D. Rueffer, A. Fontcuberta, I. Morral, D. Grundler, Magnetization reversal in individual Py and CoFeB nanotubes locally probed via anisotropic magnetoresistance and anomalous Nernst effect, *Appl. Phys. Lett.* 108, 132408 (2016).
- [124] H. Reichlova, R. Schlitz, S. Beckert, P. Swekis, A. Markou, Y. C. Chen, D. Kriegner, S. Fabretti, G. H. Park, A. Niemann, S. Sudheendra, A. Thomas, K. Nielsch, C. Felser and S. T. B. Goennenwein, Large anomalous Nernst effect in thin films of the Weyl semimetal Co_2MnGa , *Appl. Phys. Lett.* 113, 212405 (2018).
- [125] M. Yamazoe, T. Kato, K. Suzuki, M. Adachi, A. Shibayama, K. Hoshi, M. Itou, N. Tsuji, Y. Sakurai, and H. Sakurai, Spin/orbital and magnetic quantum number selective magnetization measurements for CoFeB/MgO multilayer films, *J. Phys.: Condens. Matter* 28, 436001 (2016).
- [126] W. J. Hardy, J. Yuan, H. Guo, P. Zhou, J. Lou, D. Natelson, Thickness dependent and magnetic field driven suppression of antiferromagnetic order in thin V_5S_8 single crystals, *ACS Nano*, 10, 5941-5946 (2016).
- [127] T. Zhu, P. Chen, Q. H. Zhang, R. C. Yu, and B. G. Liu, Giant linear anomalous Hall effect in the perpendicular CoFeB thin films, *Appl. Phys. Lett.* 104, 202404 (2014).
- [128] F. J. Yang, C. Wei, X. Q. Chen, Half-metallicity and anisotropic magnetoresistance of epitaxial Co_2FeSi Heusler films, *Appl. Phys. Lett.* 102, 172403 (2013).
- [129] A. Sakai, Y. P. Mizuta, A. A. Nugroho, R. Sihombing, T. Koretsune, M. T. Suzuki, N. Takemori, R. Ishii, D. Nishio-Hamane, R. Arita, P. Goswami, S.

Nakatsuji, Giant anomalous Nernst effect and quantum-critical scaling in a ferromagnetic semimetal, *Nature Physics*, 14, 1119-1124 (2018).

[130] C. Felser, B. Yan, Magnetically induced, *Nat. Mater.* 15, 1149 (2016).

[131] W. Shi, L. Muechler, K. Manna, Y. Zhang, K. Koepf, R. Car, J. van den Brink, C. Felser, Y. Sun, Prediction of a magnetic Weyl semimetal without spin-orbit coupling and strong anomalous Hall effect in the Heusler compensated, *Phys. Rev. B* 97, 060406(R) (2018).

[132] I. Belopolski, K. Manna, D. S. Sanchez, G. Chang, B. Ernst, J. Yin, S. S. Zhang, T. Cochran, N. Shumiya, H. Zheng, B. Singh, G. Bian, D. Multer, M. Litskevich, X. Zhou, S. M. Huang, B. Wang, T. R. Chang, S. Y. Xu, A. Bansil, C. Felser, H. Lin, M. Z. Hasan, Discovery of topological Weyl fermion lines and drumhead surface states in a room temperature magnet, *Science*, 20, 365 (2019).

[133] M. Jonson, G. D. Mahan, Mott's formula for the thermopower and the Wiedemann-Franz law, *Phys. Rev. B* 21, 4223 (1980).

[134] W.-L. Lee, S. Watauchi, V. L. Miller, R. J. Cava, N. P. Ong, Anomalous Hall heat current and Nernst effect in the $\text{CuCr}_2\text{Se}_{4-x}\text{Br}_x$ ferromagnet, *Phys. Rev. Lett.* 93, 226601 (2004).

[135] Y. Pu, D. Chiba, F. Matsukura, H. Ohno, J. Shi, Mott relation for anomalous Hall and Nernst effect in $\text{Ga}_{1-x}\text{Mn}_x\text{As}$ ferromagnetic semiconductors, *Phys. Rev. Lett.* 101, 117208 (2008).

[136] J. Noky, J. Gooth, C. Felser, Y. Sun, Characterization of topological band structures away from the Fermi level by the anomalous Nernst effect, *Phys. Rev. B* 98, 241106(R) (2018).

[137] D. Xiao, Y. Yao, Z. Fang, Q. Niu, Berry-phase effect in anomalous thermoelectric transport, *Phys. Rev. Lett.* 97, 026603 (2006).

[138] A. Markou, D. Kriegner, J. Gayles, L. Zhang, Y. C. Chen, B. Ernst, Y. H. Lai, W. Schnelle, Y. H. Chu, Y. Sun, C. Felser, Thickness dependence of the anomalous Hall effect in thin films of the topological semimetal Co_2MnGa , *Phys. Rev. B* 100, 054422 (2019).

[139] S. Meyer, Y. -T. Chen, S. Wimmer, M. Althammer, T. Wimmer, R. Schlitz, S. Gepraegs, H. Huebl, D. Koedderitzsch, H. Ebert, G. E. W. Bauer, R. Gross, S. T. B. Goennenwein, Observation of the spin Nernst effect, *Nature Mater.* 16, 977-981 (2017).

[140] P. J. Webster, Magnetic and chemical order in Heusler alloys containing cobalt and manganese, *J. Phys. Chem. Solids* 32(6), 1221 (1971).

- [141] R. Yu, W. Zhang, H.-J. Zhang, S.-C. Zhang, X. Dai Z. Fang, Quantized anomalous hall effect in magnetic topological insulators, *Science* 329, 61 (2010).
- [142] T. C. Chuang, P. L. Su, P. H. Wu S. Y. Huang, Enhancement of the anomalous Nernst effect in ferromagnetic thin films, *Phys. Rev. B* 96, 174406 (2017).
- [143] T. Sato, S. Kokado, S. Kosaka, T. Ishikawa, T. Ogawa M. Tsunoda, Thickness dependence of the anomalous Nernst effect and the Mott relation of Weyl semimetal Co_2MnGa thin film, *Appl. Phys. Lett.* 133, 112407 (2018).
- [144] Y. M. Lu, J. W. Cai, Z. Guo and X. X. Zhang, Unconventional scaling of the anomalous Hall effect accompanying electron localization correction in the dirty regime, *Phys. Rev. B* 87, 094405 (2013).
- [145] K. W. Edmonds, R. P. Campion, K.-Y. Wang, A. C. Neumann, B. L. Gallagher, C. T. Foxon, P. C. Main, Magnetoresistance and hall effect in the ferromagnetic semiconductor $\text{Ga}_{1-x}\text{Mn}_x\text{As}$, *J. Appl. Phys.* 93, 6787 (2003).
- [146] A. Oiwa, A. Endo, S. Katsumoto, Y. Iye, H. Ohno and H. Munekata, Magnetic and transport properties of the ferromagnetic semiconductor heterostructures $(\text{In, Mn})\text{As}/(\text{Ga, Al})\text{Sb}$, *Phys. Rev. B* 59, 5826 (1999).
- [147] T. Miyasato, N. Abe, T. Fujii, A. Asamitsu, S. Onoda, Y. Onose, N. Nagaosa Y. Tokura, Crossover behavior of the anomalous Hall effect and anomalous Nernst effect in itinerant ferromagnets, *Phys. Rev. Lett.* 99, 086602 (2007).
- [148] R. Ramos, T. Kikkawa, K. Uchida, H. Adachi, I. Lucas, M. H. Aguirre, P. Algarabel, L. Morellón, S. Maekawa, E. Saitoh M. R. Ibarra, Observation of the spin Seebeck effect in epitaxial Fe_3O_4 thin film, *Appl. Phys. Lett.* 102, 072413 (2013).
- [149] S. Onoda, N. Sugimoto, N. Nagaosa, Quantum transport theory of anomalous electric, thermoelectric, and thermal hall effect in ferromagnets, *Phys. Rev. B* 77, 165103 (2008).
- [150] K. Hasegawa, M. Mizuguchi, Y. Sakuraba, T. Kamada, T. Kojima, T. Kubota, S. Mizukami, T. Miyazaki, K. Takanashi, Material dependence of anomalous Nernst effect in perpendicularly magnetized ordered-alloy thin films, *Appl. Phys. Lett.* 106, 252405 (2015).
- [151] M. Ikhlas, T. Tomita, T. Koretsune, M. T. Suzuki, D. Nishio-Hamane, R. Arita, Y. Otani, S. Nakatsuji, Large anomalous Nernst effect at room temperature in a chiral antiferromagnet, *Nat. Phys.* 13, 1085–1090 (2017).

- [152] Y. Sakuraba, K. Hyodo, A. Sakuma, S. Mitani, Strategic enhancement of anomalous Nernst effect in $\text{Co}_2\text{MnA}_{11-x}\text{Si}_x$ Heusler compounds, <https://arxiv.org/abs/1807.02209>
- [153] J. Noky, Q. Xu, C. Felser, Y. Sun, Large anomalous Hall and Nernst effects from nodal line symmetry breaking in Fe_2MnX ($X=\text{P, As, Sb}$), *Phys. Rev. B* 99, 165117 (2019).
- [154] J. Noky, J. Gayles, C. Felser, Y. Sun, Strong anomalous Nernst effect in collinear magnetic Weyl semimetals without net magnetic moments, *Phys. Rev. B* 97, 220405(R) (2018).
- [155] G. Chang, S. Y. Xu, X. Zhou, S. M. Huang, B. Singh, B. Wang, I. Belopolski, J. Yin, S. Zhang, A. Bansil, H. Lin, M. Z. Hasan, Topological Hopf and Chain link semimetal states and their application to Co_2MnGa , *Phys. Rev. Lett.* 119, 156401 (2017).
- [156] F. Tang, Y. Ren, P. Wang, R. Zhong, J. Schneeloch, S. A. Yang, K. Yang, P. A. Lee, G. Gu, Z. Qiao, L. Zhang, Three-dimensional quantum hall effect and metal-insulator transition in ZrTe_5 , *Nature* 569, 537-541 (2019).
- [157] H. Zhang, L. M. Liu, W. M. Lau, Dimension-dependent phase transition and magnetic properties of VS_2 , *J. Mater. Chem. A* 1, 10821 (2013).
- [158] H. L. Zhuang, R. G. Hennig, Stability and magnetism of strongly correlated single-layer VS_2 , *Phys. Rev. B*, 93 054429 (2016).
- [159] Y. Qu, M. Shao, Y. Shao, M. Yang, J. Xu, C. T. Kwok, X. Shi, Z. Lu, H. Pan, Ultra-high electrocatalytic activity of VS_2 nanoflowers for efficient hydrogen evolution reaction, *J. Mater. Chem. A* 5, 15080-15086 (2017).
- [160] K. S. Nikonov, M. N. Brekhovskikh, A. V. Egorysheva, T. K. Menshchikove, V. A. Fedorov, Chemical vapor transport growth of vanadium (IV) selenide and vanadium (IV) telluride single crystals, *Inorganic Materials* 53, 1126-1130 (2017).
- [161] G. A. Wiegers, Physical properties of first-row transition metal dichalcogenides and their intercalates, *Physica B+C* 99, 151-165 (1980).
- [162] M. Mulazzi, A. Chainani, N. Katayama, R. Eguchi, M. Matsunami, H. Ohashi, Y. Senba, M. Nohara, M. Uchida, H. Takagi, S. Shin, Absence of nesting in the charge-density-wave system 1T-VS_2 as seen by photoelectron spectroscopy, *Phys. Rev. B* 82, 075130 (2010)
- [163] H. Nozaki, Y. Ishizawa, An evidence of spin flopping in V_5S_8 by magnetoresistance experiments, *Phys. Lett. A* 63, 131 (1977).

- [164] M. Nakanishi, K. Yoshimura, K. Kosuge, T. Goto, T. Fujii, J. Takada, Anomalous field-induced magnetic transition in V_5X_8 ($X=S, Se$), *J. Magn. Magn. Mater.* 221, 301 (2000).
- [165] H. Fukuyama, Effects of interactions on non-metallic behaviors in two-dimensional disordered systems, *J. Phys. Soc. Jpn.*, 48, 2169 (1980).
- [166] T. C. Chasapis, D. Koumoulis, B. Leung, N. P. Calta, S. -H. Lo, V. P. Dravid, L. S. Bouchard, M. G. Kanatzidis, Two-band model interpretation of the p- to n-transition in ternary tetradymite topological insulators, *APL Materials* 3 083601 (2015).
- [167] A. P. Lee, D. S. Fisher, Anderson localization in two dimensions, *Phys. Rev. Lett.* 47 882 (1981).
- [168] W. F. Li, C. Fang, M. A. van Huis, Strong spin-orbit splitting and magnetism of point defect states in monolayer WS_2 , *Phys. Rev. B* 94, 195425 (2016).
- [169] M. C. Wang, C. C. Huang, C. H. Cheung, C. Y. Chen, S. G. Tan, T. W. Huang, Prospects and opportunities of 2D van der Waals magnetic systems, *Annalen Der Physik*, 532(5), 1900452–19 (2020).

Declaration of Authorship

I hereby certify that this thesis has been composed by me and is based on my own work, true to my knowledge. No other person's work has been used without due acknowledgement in this thesis. All references and verbatim extracts have been quoted, and all sources of information, including graphs and data sets, have been specifically acknowledged.

Signature